

Low temperature plasticity and dislocation creep of Fangshan dolomite

Jianfeng Li¹, Tongbin Shao¹, and Mao-shuang Song²

¹Guangzhou Institute of Geochemistry (CAS)

²Guangzhou Institute of Geochemistry

November 21, 2022

Abstract

In order to explore the cause behind a recently so-called inversion of activation energy between dislocation-diffusion creep, we compress Fangshan dolomite at effective pressures of 50-300 MPa, temperatures of 27-900 °C, and strain rates of 10⁻²-10⁻¹ s⁻¹ using a Paterson-type apparatus. Two end-member deformation regimes, each with respective diagnostic flow law and microstructure, are recognized. At T < 500 °C, low temperature plasticity (LTP), expressed by an exponential constitutive equation with $\dot{\epsilon} \propto \exp(-Q/RT)$ and $\sigma \propto \dot{\epsilon}^{1/2}$, was determined with weakly strain rate dependence and thermal hardening of the strength, and microstructures of predominant undulatory extinctions or f-twinning (Regime 1). At T > 800 °C, dislocation creep, described by a power law equation ($\dot{\epsilon} \propto \sigma^n \exp(-Q/RT)$ with $n > 2$ and $\sigma \propto \dot{\epsilon}^{1/n}$), was defined with significant strain rate and temperature sensitivities of strength, and microstructures dominated by smooth undulating extinction and new recrystallized grains (Regime 2). Regime 3, transition from LTP to dislocation creep, is also recognized from ~600 °C to 800 °C with strain rate dependence of strength changing with temperature and developing microstructures similar to those of regime 2. Overall the medium-grained Fangshan dolomites show similar rheology to coarse-grained Madoc dolomites but a beginning temperature of regime 2 about 50-100 °C lower than the latter, making the dislocation creep of Fangshan dolomite clearly recognized under the condition that dolomite decomposition has no obvious effect. Extrapolated to nature, dislocation creep is expected to occur in a relatively narrow space undergoing high temperatures and relatively high stresses, instead diffusion creep is expected to dominate the deformation of dolomite in low stress tectonic settings.

1 Low temperature plasticity and dislocation creep of Fangshan dolomite

2
3 Jianfeng Li, Tongbin Shao*, Maoshuang Song**

4
5 State Key Laboratory of Isotope Geochemistry, Guangzhou Institute of Geochemistry,
6 Chinese Academy of Sciences, Guangzhou, 510640, China

7
8 **, Corresponding authors: tshao@gig.ac.cn (Tongbin Shao), msong@gig.ac.cn
9 (Maoshuang Song)

10
11 **Abstract:** In order to explore the cause behind a recently so-called inversion of
12 activation energy between dislocation-diffusion creep, we compress Fangshan dolomite
13 at effective pressures of 50-300 MPa, temperatures of 27-900 °C, and strain rates of 10^{-6} - 2×10^{-4} s⁻¹ using a Paterson-type apparatus. Two end-member deformation regimes,
14 each with respective diagnostic flow law and microstructure, are recognized. At
15 $T \leq 500$ °C, low temperature plasticity (LTP), expressed by an exponential constitutive
16 equation $\dot{\epsilon} = \dot{\epsilon}_0 \times \exp(\alpha \times \sigma)$ with $\alpha = 0.081 \pm 0.0078$ and $\ln \dot{\epsilon}_0 = -76.66 \pm 6.24$, was
17 determined with weakly strain rate dependence and thermal hardening of the strength,
18 and microstructures of predominant undulatory extinctions or f-twinning (Regime 1).

19
20 At $T \geq 800$ °C, dislocation creep, described by a power law equation ($\dot{\epsilon} = A \sigma^n \exp\left(\frac{-Q}{RT}\right)$
21 with $n = 4.75 \pm 0.58$, $Q = 436 \pm 54$ kJ/mol and $\log A = 3.48 \pm 1.41$), was defined with
22 significant strain rate and temperature sensitivities of strength, and microstructures
23 dominated by smooth undulating extinction and new recrystallized grains (Regime 2).
24 Regime 3, transition from LTP to dislocation creep, is also recognized from ~600 °C to
25 800 °C with strain rate dependence of strength changing with temperature and
26 developing microstructures similar to those of regime 2. Overall the medium-grained
27 Fangshan dolomites show similar rheology to coarse-grained Madoc dolomites but a
28 beginning temperature of regime 2 about 50-100 °C than the latter, making the

29 dislocation creep of Fangshan dolomite clearly recognized under the condition that
30 dolomite decomposition has no obvious effect. Extrapolated to nature, dislocation creep
31 is expected to occur in a relatively narrow space undergoing high temperatures and
32 relatively high stresses, instead diffusion creep is expected to dominate the deformation
33 of dolomite in low stress tectonic settings.

34

35 **Keywords:** Dolomite, Low temperature plasticity, Dislocation creep, Activation energy,
36 High temperature high pressure, Rheology

37

38 **1. Introduction**

39 Carbonates, which commonly form and accumulate in shallow-marine
40 environments along continental margins, are distributed extensively in shear zones and
41 orogenic belts in middle and upper crust, and some of them enter the deep Earth during
42 subduction [*Goto et al., 2007; Zhang et al., 2003*]. Carbonates are believed to control
43 the stresses in the middle and upper crust during continental collision by low strength
44 calcite (CaCO_3) and dolomite ($\text{CaMg}(\text{CO}_3)_2$) [e.g., *Bestmann et al., 2000; Ulrich et al.,*
45 *2002*] and play a potential role in the geodynamics of ultrahigh pressure (UHP)
46 metamorphic terranes, mantle wedge, and subduction zones by the mechanical
47 properties of magnesite (MgCO_3) [*Holyoke et al., 2014*]. Obviously, it is of great
48 importance to study the mechanical properties of all carbonates in the Mg-Ca system
49 for understanding the strain and stress distributions in the middle and upper crust and
50 deep Earth.

51 Ca end-member carbonate, calcite, Mg end-member carbonate, magnesite, and
52 their intermediate (Mg:Ca = 1:1) composition, dolomite, all have a rhombohedral
53 crystal structure with the crystal symmetry ($R\bar{3}c$) of the two end-members distinct
54 from that ($R\bar{3}$) of the intermediate. The similarity and difference of crystal structure
55 and symmetry of the three carbonates imply that mechanical properties of the end-
56 members may be comparable and the flow strength of the three carbonates are expected
57 to related to their magnesium content and shear moduli [*Holyoke et al., 2014*].

58 Rheological behaviors and deformation mechanisms of calcite aggregates have
59 attracted extensive research interest [e.g., *Austin and Evans, 2009; de Bresser, 2002; de*
60 *Bresser et al., 2005; Freund et al., 2004; Gratier et al., 2011; Griggs and Miller, 1951;*
61 *Griggs et al., 1953; Handin and Griggs, 1951; Heard and Raleigh, 1972; Herwegh et*
62 *al., 2003, 2005; Renner et al., 2002; Rutter, 1972, 1974; Rybacki et al., 2011, 2013;*
63 *Schmid et al., 1977, 1980; Song et al., 2014; Turner et al., 1956; Walker et al., 1990;*
64 *Xu et al., 2009, 2010; Zhang and Zhou, 2012; Zhang et al., 2017*]. Of these, the strength
65 of calcite deformed by dislocation creep increased with increasing magnesium content
66 [*Xu et al., 2009*], implying that in the dislocation creep regime the Mg end-member
67 carbonate, magnesite, should be stronger than the intermediate, dolomite, which instead
68 should be stronger than the Ca end-member carbonate, calcite. This was proved recently
69 by *Holyoke et al. [2014]* in which magnesite was shortened in both Heard gas-medium
70 apparatus and Griggs-type solid-medium apparatus to determine its three deformation
71 mechanisms (Low temperature plasticity (LTP), diffusion creep, and dislocation creep)
72 and corresponding flow laws [*Holyoke et al., 2014*]. In contrast to magnesite, although
73 much more high temperature deformation experiments were performed on single
74 crystals [e.g., *Barber and Wenk, 1979, 2001; Barber et al., 1981*] and polycrystalline
75 aggregates [e.g., *Davis et al., 2008; Delle Piane et al., 2008; Heard, 1976; Holyoke et*
76 *al., 2013; Neumann, 1969*] of the intermediate, dolomite, there are some debates or
77 doubts. For example, in order to determine the rheological behavior and flow law of
78 coarse-grained dolomite aggregates deformed by dislocation creep, *Holyoke et al.*
79 *[2013]* performed a series of triaxial compression deformation in a modified-type
80 Griggs apparatus and obtained a significantly low activation energy ($Q=145$ kJ/mol)
81 for dislocation creep [*Holyoke et al., 2013*] relative to that ($Q=410$ kJ/mol) for
82 dislocation creep with assuming $n=7$ and that ($Q=280$ kJ/mol) for diffusion creep
83 [*Davis et al., 2008*]. Notably, there is a large discrepancy in activation energy for
84 dislocation creep determined from these two studies, and such large difference also
85 occurs in activation energy of dislocation creep between the two end-member
86 carbonates and the intermediate. For this, however, there is no a reasonable
87 interpretation. In addition, such an inversion of activation energy between dislocation

88 and diffusion creep is obviously unusual since it is generally accepted that rate-limiting
89 mechanisms of intracrystalline deformation will be controlled by larger energy
90 landscape (activation barriers) relative to grain boundary processes such as grain
91 boundary sliding and diffusion creep. It is therefore necessary to perform further
92 research to explore the rate-limiting processes of diffusion and dislocation creep of
93 dolomite, thereby helping us to understand the cause behind the inversion of activation
94 energy.

95 In this study, we performed a set of triaxial compression experiments at effective
96 confining pressures of ~50-300 MPa, temperatures of 27-900 °C and strain rates of 10^{-6} - 2×10^{-4} s⁻¹ in a Paterson-type apparatus to explore the deformation mechanisms and
98 rheological behaviors of medium-grained Fangshan dolomite polycrystalline
99 aggregates.

100

101 **2. Experimental Methods**

102 A series of triaxial compression experiments were conducted to determine the
103 dependences of flow stress on strain rate and temperature. Microstructures of dolomite
104 aggregates before and after deformation were identified in ultra-thin polished sections
105 (~10 μm) by a Leica optical microscope to document the deformation mechanisms.

106 **2.1. Starting Materials**

107 A white Fangshan dolomite block was collected from a quarry locating in Shiwo
108 town, Fangshan district, Beijing, China. The block is of homogenous structure without
109 obvious mineral bands or foliations, and comprised of primary dolomite (>97 vol.%),
110 secondary calcite, mica and apatite. Chemical compositions were obtained by an EMP
111 analysis with a stoichiometric molecular formula of Mg/Ca ratios between 0.97 and
112 1.02 (Table 1). Optical examination on this material (Figure 1a) displays approximately
113 equant grains with diameter determined as 113 ± 42 μm by linear traverses of the thin
114 section under optical microscopy (Figure 1b). As shown in Figure 1a, sharp boundaries,
115 uniform extinction and some straight boundary twin can be observed, and negligible
116 porosity of less than 1% can be estimated. Neither banding nor foliation has been
117 observed in hand specimen, but pole figures (Figure 2) generated by Electron

118 Backscatter Diffraction (EBSD) analysis display a weak initial fabric with maximum
119 c-axis densities about two times the expected mean density for random distributions.

120 **2.2. Sample Preparation and Jacketing**

121 Specimen cylinders of 10 mm diameter and 20 mm length were core-drilled from
122 a block of the Fangshan dolomite. The top and bottom surfaces of the cylinders were
123 polished to roughness of less than $\pm 5 \mu\text{m}$. Before each test, the cylindrical specimens
124 were dried for at least 24 hours in an oven at 110 °C in order to drive away free water,
125 and then sandwiched between 3 mm thick solid alumina spacers, additional 58 mm long
126 alumina and 30 mm long zirconia pistons to insure a good thermal profile along the
127 longitudinal direction of sample (Figure 3). The assembly was sealed in low carbon iron
128 jackets with 0.25 mm wall thickness and 15 mm inner diameter in order to isolate the
129 sample from the confining medium of argon gas. In the central part glued to the
130 specimen, the jacket was swaged down to 10 mm, which resulted in local thickening up
131 to a maximum of ~ 0.4 mm.

132 **2.3. Deformation Experiments**

133 The triaxial compression experiments were performed on dolomite aggregates
134 under ~ 50 -300 MPa effective confining pressure and ~ 27 -900 °C temperatures in an
135 internally heated Paterson gas-medium (argon) deformation apparatus [Paterson, 1970;
136 Shao et al., 2011]. The temperature distributions inside the furnace were regularly
137 calibrated to make sure that the thermal profiles were nearly constant (within ± 2 °C)
138 along the longitudinal direction of sample. Temperatures were monitored by a R-type
139 (Pt13%Rh-Pt) thermocouple placed about 3 mm above the top surface of the specimen.
140 Temperature was increased at a rate of 20 °C per minute to the testing temperature, and
141 then maintained 30 minutes for equilibrium. Details of the deformation apparatus and
142 data processing can refer to Shao et al. [2011] and Li et al. [2013], respectively. In order
143 to obtain the flow laws and explore the rheological behaviors of dolomite, two types of
144 tests were employed:

145 (1) Constant strain rate tests. Indeed, we drive the motor at a constant displacement
146 speed during the whole deformation process. Since a constant flow stress was soon
147 approximately reached after a transient elastic period (generally less than about 3%

148 strain) in most tests, the main part of the test was at approximately constant strain rate.

149 (2) Strain-rate-stepping tests. The stepping tests comprise of a series of steady flow
150 at various strain rates. Generally, we performed these tests by abruptly increasing the
151 strain rate after the specimen had settle down to a steady flow at the previous strain rate.

152 The testing conditions (include temperature, confining pressure, and strain rate)
153 and mechanical results of the experiments were listed in [Tables 2](#) and [3](#), respectively,
154 for the constant strain rate tests and steeping tests. For specimens deformed at relatively
155 low temperatures and without undergoing strain-weakening, differential stresses at 5%
156 strains were adopt as flow stresses of the specimens. If the total strain for the constant
157 strain rate tests or each step of stepping tests was less than 5%, a power function used
158 to fit the strain hardening after yield point can be written as

$$159 \quad \sigma = A \times (\varepsilon - b)^m$$

160 and extrapolated to 5 % strain where differential stress was read and considered as
161 flow stress. In the function, σ and ε are real-time differential stress and strain,
162 respectively; A , b and m are fitting parameters and m is closely related to the strain
163 hardening degree of the specimen. For specimens undergoing strain weakening at
164 high temperature, however, peak differential stresses were considered as flow stresses.

165 Additionally, as the ceramic spacers beneath the specimen were solid without
166 central hole, the gas produced by dolomite decomposition (generates calcite, periclase
167 and CO_2) at high temperatures ($\geq \sim 700$ °C) could not escape from the assembly and
168 thus generated pore fluid pressure. As mentioned above, the porosity of the starting
169 material (Fangshan dolomite) was less than 1%, little decomposition at grain surfaces
170 of the dolomite would reach equilibrium. Hence, the stability of the dolomite can be
171 maintained in the laboratory on the basis of the above facts and microstructure
172 observations. According to the decomposition reaction equilibrium of dolomite
173 presented by [Goldsmith \[1959\]](#), CO_2 pore pressure at different temperatures could be
174 obtained, and the effective confining pressure could be expressed by

$$175 \quad P_e = P_c - P_{\text{CO}_2}$$

176 where P_e , P_c and P_{CO_2} represent the effective confining pressure, confining

177 pressure and pore fluid pressure generated by CO₂, respectively.

178 As the confining pressure of tests in this work were mostly fixed at ~300 MPa, the
179 effective confining pressure would be various once the decomposition of the dolomite
180 grains occurred at different deformation temperatures. In order to obtain flow stress
181 corresponding to a constant confining pressure (P_c) for building constitutive equation,
182 the following corrections should be emphasized:

183 It was suggested by *Davis et al. [2008]* that flow stress of Madoc dolomite depends
184 linearly on effective confining pressure with tiny apparent coefficient of inner friction
185 about 0.1 ($\mu \cong 0.1$) if deformed at $P_e > 100$ MPa, 700 °C and strain rate of 1.25×10^{-5}
186 s^{-1} , while if $P_e < 100$ MPa the dependence of flow strength on effective confining
187 pressure met Mohr – Coulumb Criterion with apparent coefficient of inner friction
188 about 1.0 ($\mu \cong 1.0$) (*Figure 4*). Similar dependent relationships were also reported in
189 other studies [e.g., *Austin and Kennedy, 2005; Austin et al., 2005; Handin and*
190 *Fairbairn, 1955; Turner et al., 1954*]. Our experimental results of samples FS34 and
191 FS26 deformed at $P_e > 100$ MPa, 800 °C and strain rate of $10^{-5} s^{-1}$ indicate that flow
192 strengths of Fangshan dolomite have a similar dependent relationship on effective
193 pressure to Madoc dolomite. Accordingly, for tests in which dolomite decomposed, if
194 $P_e \geq 100$ MPa, the flow strength was corrected by:

$$195 \quad \sigma_t = \sigma_{5\%} + 0.1 \times (300 - P_e) \quad (1)$$

196 where σ_t is the true flow strength corresponding to effective confining pressure of
197 300 MPa; $\sigma_{5\%}$ is the differential stress read at 5% strain; P_e is the effective confining
198 pressure. If $P_e < 100$ MPa, the true flow strength can be obtained by:

$$199 \quad \sigma_t = \sigma_{5\%} + (100 - P_e) + 0.1 \times (300 - 100) \quad (2)$$

200 The corrected flow stress corresponding to effective confining pressure of 300 MPa was
201 filling into antepenultimate column of *Tables 2* and *3*.

202 At last, power law and exponent law constitutive equations were fitted to the
203 mechanical data of the tests at higher and lower temperatures, respectively.

204 **2.4. Microstructure Observations**

205 Specimens deformed at various strain rates and temperatures were inspected to
206 characterize their deformation microstructures by a Leica microscopy in parallel-
207 polarized light and cross-polarized light. The specimens were impregnated with an
208 epoxy resin and then cut in half along the compression direction. One half was polished
209 to thin sections of about 10 μm thick. Microcracks can be judged in parallel-polarized
210 light micrographs. In contrast, mechanical twinning, undulating extinctions,
211 deformation bands and recrystallization grains can be observed in cross-polarized light
212 micrographs.

213

214 **3. Results**

215 **3.1. Mechanical Data**

216 The mechanical results of constant strain rate and strain-rate-stepping tests are
217 listed in [Tables 2](#) and [3](#), respectively. Differential stress versus strain curves for constant
218 strain rate and strain-rate-stepping tests are displayed in [Figures 5](#) and [6](#), respectively.
219 According to strain rate and temperature dependences of flow stress, three deformation
220 regimes have been distinguished by temperature bounds as follows:

221 **Regime 1 (≤ 500 °C).** In this regime, the Fangshan dolomites yield when
222 differential stresses lie between ~ 352 and 501 MPa at strains 0.5% - 1% . Once reaching
223 yield point, the differential stress versus strain curves ([Figures 5](#) and [6](#)) deviate from
224 linear relationship and show various degrees of strain hardening (depending on
225 temperature). It was found that specimens deformed at 500 °C had the most obvious
226 strain hardening ([Figure 5a](#)). Differential stresses at 5% strain of sample deformed in
227 regime 1 arrive between ~ 765 and 832 MPa. Flow stresses show weak dependences on
228 temperature and strain rate ([Figure 5a](#)). For instance, the increase of flow stresses with
229 strain rate increasing were too slight to escape from being covered up by strain
230 hardening and/or strength discrepancy likely resulting from microstructure difference
231 among specimens. Thus, it is necessary for strain-rate-stepping tests being carried out
232 on a single specimen to eliminate the effect of microstructure discrepancy. From
233 logarithmic graph of strain rate versus flow stress ([Figure 7a](#)), linear dependent
234 relationships with dramatically steep slopes (apparent n) of 70 - 78 were identified.

235 Increasing experimental temperatures from room temperature to 300 °C, flow strengths
236 of the Fangshan dolomite become weakly lower or nearly invariant; while increasing
237 temperatures from 300 °C to 500 °C, the flow strengths increase slightly (Figure 8).
238 This unusual temperature dependence cannot be described by an Arrhenius relationship.
239 Thus, an exponential law without Arrhenius factor:

$$\dot{\epsilon} = \dot{\epsilon}_0 \times \exp(\alpha \times \sigma_{5\%}) \quad (3)$$

241 was used to fit the mechanical results in regime 1. In equation (3), $\dot{\epsilon}$ is strain rate, pre-
242 exponential terms $\dot{\epsilon}_0$ is in units of strain rate (s^{-1}), $\sigma_{5\%}$ is the differential stress read
243 at 5% strain, α (MPa^{-1}) is fitting parameter. By multiple least square fitting of
244 experimental results at room temperature to 300 °C, parameters in equation (3) can be
245 determined as $\alpha = 0.081 \pm 0.0078$ and $\ln \dot{\epsilon}_0 = -76.66 \pm 6.24$. Fitting of mechanical
246 data of 500 °C gives nearly same α ($= 0.084$) and $\ln \dot{\epsilon}_0$ ($= -80.23$).

247 **② Regime 2 (≥ 800 °C).** This regime refers to experiments at temperatures higher
248 than 800 °C and/or low strain rate ($\leq 1.0 \times 10^{-5} \text{ s}^{-1}$) at 800 °C, and is characterized by low
249 flow stresses not higher than ~520 MPa. In this regime, the yield strengths of Fangshan
250 dolomite were much lower, strain hardening after the yield point was inconspicuous,
251 instead strain weakening on differential stress versus strain curves are observed after
252 ~3%-6% strain (Figures 5c and 5d). At $T=850$ °C, strain weakening of dolomite is
253 generally prominent with significant stress drop occurring at strains of ~3%-4%.
254 Corrected flow strengths of Fangshan dolomite are 204 to 518 MPa, and increase much
255 more significantly with increasing strain rates, apparently different from regime 1. In
256 the logarithmic diagram of strain rate versus differential stress, flow strengths of
257 constant strain rate experiments (peak stresses of each test) are consistent well with that
258 of strain-rate-stepping experiments where differential stresses are read for each step as
259 near as possible to 5% strain although some scatter may be present. Linear relationships
260 between strain rate and flow strength have more gentle slopes of 3.8 – 5.4 (Figure 7c),
261 basically consistent with the expected values of stress exponent for dislocation creep.
262 Increasing or decreasing temperature, flow strengths decrease or increase more

263 obviously than those for samples deformed at temperature lower than 600 °C. In a
 264 diagram of logarithmic flow strength versus $1000/T$ (Figure 8a), significant positive
 265 linear dependence of steeply inclined slope ($\rho = \frac{Q^* \log \sigma}{nR} = 4.82 - 4.86$ in Figure 8b)
 266 is determined at high temperatures (≥ 800 °C), obviously different from the
 267 approximately horizontal slope at temperatures lower than 600 °C.

268 Power law with Arrhenius factor could describe well the rheological behavior at
 269 high temperatures with the formation as:

$$270 \quad \dot{\epsilon} = A \times \sigma^n \exp\left(\frac{-Q}{RT}\right) \quad (4)$$

271 where $\dot{\epsilon}$ is strain rate, A is the pre-exponential term, R is the gas constant, Q is the
 272 active energy, T is absolute temperature in K, n is fitting parameter indicative of stress
 273 exponent, and σ is the flow stress corresponding to $P_e = 300$ MPa in this study. For
 274 individual constant strain rate experiments, peak stresses are adopted as flow stresses;
 275 while in strain-rate-stepping experiments differential stresses read at strains as near as
 276 possible to 5% are considered as flow stresses of each step. By multiple least square
 277 fitting of experimental results of flow stresses lower than 520 MPa, parameters in
 278 equation (4) can be determined as $n = 4.75 \pm 0.58$, $Q = 436 \pm 54$ kJ/mol and $\log A = 3.48 \pm 1.41$.

279 A transitional regime (Regime 3) from regime 1 to regime 2 is also recognized at
 280 temperatures between 500 °C and 750 (800) °C. In this regime, increasing strain rate,
 281 flow stresses will increase more significantly than in regime 1 but not as significantly
 282 as in regime 2. Lower than regime 1 but higher than regime 2, the slopes of linear
 283 relationship between logarithmic strain rate and logarithmic flow stress for the
 284 transitional regime range from 48 to 13 (11) (Figure 7b). A corresponding transitional
 285 stress dependence on temperature can also be recognized in Figure 8a, indicated by
 286 cambered distribution of data points. As the apparent n values are much higher than the
 287 values expected for dislocation creep [$3 \leq n \leq 5$, Poirier, 1985] and decrease with
 288 increasing temperature, the deformation mechanism of the regime 3 should be
 289 dominated by dislocation glide with little effect of recovery on dislocation creep, the
 290 process transition from grain boundary sliding to high temperature intracrystalline

291 plasticity.

292 **3.2. Microstructures**

293 The deformation microstructures of Fangshan dolomite at the optical scale are
294 distinguished briefly in the above three deformation regimes.

295 (1) Specimens deformed in regime 1 (≤ 500 °C)

296 Optical observations reveal a preponderance of mechanical twinning (Figures 9c-
297 9f) in this regime. The twins produced by deformation were of lensoid shape, with sharp
298 ends at grain boundaries. This characteristic lamellae shape makes them easily
299 distinguishable from the straight lamellae boundaries which may be initially present or
300 produced by quenching during cooling and depressurizing at the end of the experiment.
301 Besides twinning, some grains show undulatory extinction (Figures 9a, 9b, and 9d). The
302 mutual developments of mechanical twinning and undulatory extinction indicate the
303 dolomite is deformed by a combination of twinning and dislocation slip. In more detail,
304 specimen deformed at room temperature is characterized by patchy undulatory
305 extinction with small amount of twins. With increasing temperature, the population of
306 twins increases. For instance, specimens at 300 °C develop much more abundant
307 deformation twins, while the most popular twins are discovered in specimens deformed
308 at 500 °C. The differential stresses reached at low temperatures ≤ 500 °C are much
309 higher than the confining pressures, brittle processes thus may contribute to
310 deformation of dolomite according to the Goetze criteria [Karato, 2008]. However, no
311 more significant micro-cracks than the starting materials have been ferreted out.

312 (2) Specimens deformed in regime 2 (≥ 800 °C)

313 Fangshan dolomites deformed at temperatures ≥ 800 °C have smooth undulatory
314 extinctions (Figures 10a-10b) and similar twin density with the starting materials. Some
315 dust like fine grains is discovered at the triple junction of dolomite grains or surrounding
316 the accessory minerals such as mica and apatite (Figures 10c). EMP analyses suggest
317 that these new grains are formed due to the lost MgO content of dolomite, consistent
318 with decomposition products of dolomite in a previous study by *Delle Piane et al.*
319 [2008]. The present of these new fine grains indicates that CO₂ has been released from
320 some old grains. As the reaction areas are less than 2% in our samples, however,

321 differential stresses measured earlier in the experiments should be able to represent the
322 flow stresses of the dolomite after corrected. Along some old and coarse dolomite grains,
323 fine grains with equiaxed polygonal shape are also discovered, which should be the
324 recrystallized new grains formed by dislocation climb and distinguished from reaction
325 products with coarser grain size and colorful optical character (Figure 10d).

326 (3) Specimens deformed in regime 3 ($\sim 500\text{ }^{\circ}\text{C} < T < 800\text{ }^{\circ}\text{C}$)

327 Specimens deformed at temperatures from $500\text{ }^{\circ}\text{C}$ to $800\text{ }^{\circ}\text{C}$ have similar
328 microstructures to those deformed at temperatures higher than $800\text{ }^{\circ}\text{C}$ with the
329 exception of no or less new fine grains generated by decomposition of dolomite.

330

331 **4 Discussion**

332 Dolomite has similar crystal structure to calcite and magnesite, with half Ca
333 octahedron in calcite replaced orderly by Mg octahedron or with half Mg octahedron in
334 magnesite replaced orderly by Ca octahedron. Experimental studies of rheological
335 properties of dolomite are much less than calcite, but much more compared to
336 magnesite. However, disputes or doubts on the rheology of dolomite are attractive. In
337 the last century, most experimental studies on dolomite deformation were performed at
338 low temperatures ($< 500\text{ }^{\circ}\text{C}$) [e.g., *Barber et al., 1994; Handin and Fairbairn, 1955;*
339 *Turner et al., 1954*], but there are some exceptions. Although at a much higher
340 temperature ($1000\text{ }^{\circ}\text{C}$), for instance, *Neumann [1969]* suggested that dislocation creep
341 was the dominant deformation mechanism of coarse-grained ($\sim 700\text{ }\mu\text{m}$) dolomite
342 aggregates based on microstructural evidences obtained, he did not determine flow laws
343 of dolomite due to poor precision of strong solid-media assemblies in the Griggs-type
344 deformation apparatus. Using high-precision gas-medium Heard and modified-type
345 Griggs apparatus, deformation experiments on coarse-grained Madoc dolomite and
346 fine-grained synthetic dolomite aggregates were carried out recently at temperatures
347 higher than $700\text{ }^{\circ}\text{C}$ [*Davis et al., 2008; Delle Piane et al., 2008; Holyoke et al., 2013*].
348 These previous studies could be compared mutually with similarity and difference both
349 in yield strength and flow strength between different studies [e.g., *Barber et al., 1994;*
350 *Davis et al., 2008; Handin and Fairbairn, 1955; Turner et al., 1954*]. For comparison,

351 some differential stress versus strain curves documented by these previous studies were
352 also plotted in [Figure 5a](#) according to their deformation temperatures. At low
353 temperatures of ≤ 300 °C, Hasmark dolomite [[Handin and Fairbairn, 1955](#)] and Crevola
354 dolomite [[Barber et al., 1994](#)] display flow strength increasing with decreasing
355 temperature. The same is true for our Fangshan dolomite deformed at temperatures
356 ≤ 300 °C, where at the same strain rate (10^{-5} s $^{-1}$) sample FS5 deformed at room
357 temperature is stronger than sample FS7 shortened at 300 °C ([Figure 5a](#)). This is also
358 true for samples compressed at temperatures ≥ 500 °C. For instance, the flow strength
359 of sample FS8 deformed at 500 °C and 7.8×10^{-6} s $^{-1}$ is much higher than that of sample
360 FS10 deformed at 700 °C and 1.7×10^{-6} s $^{-1}$. From 300 °C to 500 °C, however, an unusual
361 increase in flow strength of Fangshan dolomite occurs with increasing temperature
362 ([Figure 5a](#)), which is similar with the dependence of flow strength of coarse-grained
363 Madoc dolomite on temperature at low temperatures ≤ 700 °C (see [Figure 2b](#) of [Davis](#)
364 [et al. \[2008\]](#)). At relatively low temperatures (≤ 500 °C), in addition, the the Fangshan
365 dolomites yield at 352–369 MPa and their flow stresses are 765–804 MPa when
366 deformed at 300 °C, while the Hasmark dolomites shortened by [Handin and Fairbairn](#)
367 [[1955](#)] yield at 364 MPa and have a flow stress of 660 MPa. This inversion of strength
368 of coarse-grained and finer-grained dolomite also occurs between the medium-grained
369 Fangshan dolomite (FS8) and coarse-grained Madoc dolomite (MD26) when deformed
370 at low temperatures ([Figure 5a](#)). When compared to previous studies, [Davis et al. \[2008\]](#)
371 also found this strength inversion that the fine-grained synthetic dolomite is stronger
372 than the coarse-grained Madoc dolomite at a temperature of 600 °C, and the fine-
373 grained Blair dolomite exhibits flow strength much higher than the coarse-grained
374 Madoc dolomite at temperatures ≤ 500 °C. Thus, these comparisons suggest that the
375 fine-grained dolomite was stronger than the coarse-grained dolomite, at relatively low
376 temperatures (≤ 500 °C for the comparisons of Fangshan or Blari dolomite with Madoc
377 dolomite, and ≤ 600 °C for those of fine-grain synthetic dolomite with Madoc dolomite).
378 Additionally, the insensitivity of flow strength to the strain rate occurs at temperatures
379 (≤ 500 °C) for our medium-grained Fangshan dolomite about 200 °C lower than those
380 (≤ 700 °C) for the coarse-grained Madoc dolomite [[Davis et al., 2008](#)]. This

381 insensitivities result in abnormally large stress exponents ($n \sim 70$ for Fangshan
382 dolomite and ~ 46 for Madoc dolomite) for these low temperature deformation
383 experiments.

384 **4.1. Deformation Mechanisms and Flow Laws**

385 Microstructure observations of the deformed specimens suggested that dislocation
386 glide is the most important deformation mechanism at room temperature to 300 °C,
387 while f-twin slip became more dominant at 300-500 °C. At temperatures $> \sim 700$ °C,
388 dislocation creep became the dominant deformation mechanism. In the light of the
389 critical resolved shear stress (CRSS) of dolomite single crystal [Figure 11; Barber *et*
390 *al.*, 1981; Higgs and Handin, 1959], at temperatures lower than 500 °C CRSS for c slip
391 was the lowest, at temperatures from 500 °C to 700 °C CRSS for f-twin slip became the
392 lowest one, while at temperatures higher than 700 °C CRSS for f slip turns to be the
393 lowest. Thus, the transient of deformation mechanism of Fangshan dolomite from c slip
394 at room temperature to f-twinning at 500 °C was consistent with the trending in change
395 of CRSS of single crystal dolomite. Deformed by dislocation glide and f-twinning at
396 low temperatures ≤ 500 °C, strength inversion of fine-grained dolomite and coarse-
397 grained dolomite is consistent with a generally accepted theory that grain boundaries
398 impede dislocation motion, and at least at lower temperatures, finer grain size (larger
399 grain boundary area) usually results in higher strength [e.g., Wright, 2016]. However,
400 mechanical data at temperatures higher than 700 °C show that the deformation
401 mechanism of Fangshan dolomite is dominated by dislocation creep instead of f slip.
402 At temperatures ≥ 800 °C, the dependence of flow stress on temperature was much more
403 significant than that of CRSS of f-slip (Figure 11), also suggesting that recovery may
404 play an important role in the deformation of the Fangshan dolomite. Furthermore, the
405 CRSSs for both c- and f-twin slips increase with temperature increasing, that is the
406 reason why the flow strength of Fangshan dolomite show slightly overall ascending
407 tendency from room temperature to 500 °C.

408 Previous studies have recognized several deformation and recovery mechanisms
409 by TEM analysis of single crystal and polycrystalline aggregate of dolomite [e.g.,
410 Barber *et al.*, 1981, 1994; Barber and Wenk, 2001]. In Crevola dolomite, for instance,

411 f twin has been observed at $25\text{ }^{\circ}\text{C}\leq T\leq 500\text{ }^{\circ}\text{C}$, $\dot{\epsilon}=10^{-4}\text{ s}^{-1}$ and $700\text{ }^{\circ}\text{C}\leq T\leq 900\text{ }^{\circ}\text{C}$, $\dot{\epsilon}=10^{-6}\text{ s}^{-1}$
 412 [*Barber et al.*, 1994]. However, the densest f twin was found to develop in the
 413 temperature range from $500\text{ }^{\circ}\text{C}$ to $700\text{ }^{\circ}\text{C}$. In contrast, c slip and f slip were active at all
 414 of temperatures, and f slip became more active at temperatures $\geq 700\text{ }^{\circ}\text{C}$. All of these
 415 observations were consistent with the mechanical data and microstructures of the
 416 Fangshan dolomite. In conclusion, intracrystalline plasticity deformation at high
 417 stresses and low temperatures $\leq 500\text{ }^{\circ}\text{C}$ should be dominated by the coaction of f–twin
 418 and c–slip; the drastic strength decrease at temperature $\geq 700\text{ }^{\circ}\text{C}$ was likely resulted
 419 from the CRSS decrease of f – slip as well as the activation of dislocation recovery.

420 The flow laws of dolomite aggregates were reported with the constitutive equation
 421 for diffusion creep with $n = 1.28$, $H^*=280\text{ kJ/mol}$ [*Davis et al.*, 2008] and $n=1.3$, $H^*=368$
 422 kJ/mol [*Delle Piane et al.*, 2008], respectively. However, an activation energy of 310
 423 kJ/mol was obtained by *Holyoke et al.* [2013] from Figure 7 of *Delle Piane et al.* [2008].
 424 Thus, the data on flow laws of diffusion creep determined by these two studies are
 425 essentially the same within experimental errors. Report about LTP and dislocation creep
 426 was scarce. *Davis et al.* [2008] experimentally studied the deformation of coarse-grained
 427 Madoc dolomite from $400\text{ }^{\circ}\text{C}$ to $850\text{ }^{\circ}\text{C}$. Exponential law with $\alpha = 0.079\pm 0.01\text{ MPa}^{-1}$ and
 428 power law with $n=26\pm 6$ and $\frac{H^*}{n} = 60\pm 6\text{ kJ/mol}$ were obtained to describe the LTP
 429 and dislocation creep of dolomite, respectively. Because the stress exponent was
 430 abnormally high for dislocation creep, *Davis et al.* [2008] adopted the n value ($n=7$) of
 431 Carrara marble [*Schmid et al.*, 1980] to calculate the activation enthalpy of the Madoc
 432 dolomite, by which a more reasonable value of $H^*\sim 410\text{ kJ/mol}$ was gotten. However,
 433 another suit of parameters of $n=3.0\pm 0.1$ and $H=145\text{ kJ/mol}$ was reported recently by
 434 *Holyoke et al.* [2013] for dislocation creep. How does such a large difference in
 435 activation energy occur between the two studies? Detail experimental works in this
 436 study show that:

437 1) The stress exponent for the Fangshan dolomite deformed at $850\text{ }^{\circ}\text{C}$ is
 438 determined as 3.8 (Figure 7c), nearly consistent with the stress exponent value
 439 ($n=3.0\pm 0.1$) obtained for Madoc dolomite deformed at $900\text{ }^{\circ}\text{C}$ by *Holyoke et al.* [2013].

440 According to the dislocation creep theories [Poirier, 1985], the deformation of
441 Fangshan dolomite at 850 °C is controlled by a dislocation creep dominant deformation
442 process. For this reason, a beginning temperature of dislocation creep may be lower for
443 the medium-grained Fangshan dolomite relative to the coarse-grained Madoc dolomite.

444 2) Overall fitting of data points of logarithmic strain rate and logarithmic stress for
445 the Fangshan dolomite deformed at 800 °C generates a value of $n=7.8$, almost equal to
446 the stress exponent value assumed previously for the dislocation creep of Madoc
447 dolomite by Davis *et al.* [2008]. At 800 °C, however, respective fitting of data points
448 for flow strengths higher than 520 MPa and lower than 520 MPa produces $n = 11.3$ and
449 $n = 5.4$, respectively. This means that the deformation of dolomite at 800 °C should be
450 mixture of regime 2 dislocation creep - dominant deformation and regime 3 dislocation
451 slip - dominant deformation. For the deformation of coarse-grained Madoc dolomite,
452 same n value ($n=49$) was reported for experiments at 600 and 700 °C, while a lower n
453 value ($n=26$) was required to fit the mechanical data at 800 °C, implying a possible
454 transition of deformation mechanism at 800 °C [Davis *et al.*, 2008]. However, the stress
455 exponent ($n=7$) assumed by Davis *et al.* [2008] for the deformation of the coarse-
456 grained Madoc dolomite at this temperature is still large relative to the values ($n=3-5$)
457 expected for dislocation creep. This is why Holyoke *et al.* [2013] obtained $n=3$ of the
458 coarse-grained Madoc dolomite only at a higher temperature ($T=900$ °C). In contrast, a
459 decrease in stress exponent of Fangshan dolomite with increasing temperature occurs
460 from 600 °C to 750 °C at which the stress exponent value ($n=13$) is nearly equal to that
461 ($n=11$) at 800 °C where flow strength is higher than 520 MPa (Figure 7b). Therefore, it
462 is suggested that the beginning temperature of dislocation creep for medium-grained
463 Fangshan dolomite is about 50-100 °C lower than that for coarse-grained Madoc
464 dolomite.

465 3) Fitting of data points of logarithmic strain rate and logarithmic stress for flow
466 strength lower than 520 MPa gives $n = 5.4$ for deformation of dolomite at 800 °C and
467 low strain rate and $n = 3.8$ for that at temperatures ≥ 850 °C. These n values are basically
468 in the range of stress exponent values expected for dislocation creep ($n = 3-5$). Therefore,
469 the deformation under differential stress less than 520 MPa should be dominated by

470 dislocation creep. Global fitting of power flow law to mechanical data with differential
471 stresses less than 520 MPa shows $n=4.75\pm 0.58$, $Q=436\pm 54$ kJ/mol and $\log A=3.48\pm 1.41$,
472 which can be used to describe the dislocation creep of the Fangshan dolomite. Stress
473 exponent and activation energy obtained here may be more reasonable according to the
474 following analyses. Firstly, as an intermediate of carbonate in Ca-Mg system, dolomite
475 has a similar crystal structure to the two end-member carbonates, calcite and magnesite.
476 Therefore, similarity in both flow laws and deformation mechanisms may be present
477 among these three carbonates. Secondly, the stress exponent (n) value of the medium-
478 grained Fangshan dolomite is roughly consistent with the value of Carrara marble
479 ($n=4.2$) [*Schmid et al., 1980*] and is within the value of stress exponent expected for
480 dislocation creep, although it is slightly higher than that of coarse-grained Madoc
481 dolomite ($n=3.0\pm 0.1$) [*Holyoke et al., 2013*]. Thirdly, the activation energy (Q)
482 determined for the medium-grained Fangshan dolomite is comparable to the values of
483 Q for Carrara marble ($Q=428$ kJ/mol) [*Schmid et al., 1980*] and magnesite ($Q=410$
484 kJ/mol) [*Holyoke et al., 2014*], but is much higher than the value determined for the
485 dislocation creep of coarse-grained Madoc dolomite ($Q=145$ kJ/mol) [*Holyoke et al.,*
486 *2013*]. Furthermore, the activation energy obtained by *Holyoke et al. [2013]* is much
487 lower than the value for diffusion creep of dolomite ($H^*\sim 248$ kJ/mol) [*Davis et al.,*
488 *2008*]. In addition to a complicated interpretation, a mechanism suggested by *Barber et*
489 *al. [1981]* responsible for anomalous hardening of c slip with increasing temperature in
490 the field of crystal plasticity was cited to link with the unusually low activation energy
491 for the dislocation creep deformation of dolomite [*Holyoke et al., 2013, 2014*]. However,
492 c slip leading to anomalous thermal hardening of dolomite is restricted at low
493 temperatures, such as at $T\leq 500$ °C for Fangshan dolomite (*Figure 5a*), rather than at
494 high temperatures where dislocation creep may dominate. In contrast to the much lower
495 activation energy determined by *Holyoke et al. [2013]*, the value of activation energy
496 for dislocation creep of Fangshan dolomite in this study is higher than those for
497 diffusion creep determined by *Davis et al. [2008]* and *Delle Piane et al. [2008]*,
498 consistent with a generally accepted knowledge that rate-limiting processes of
499 intracrystalline creep will be controlled by larger energy landscape (activation barriers)

500 relative to grain boundary process such as grain boundary sliding and diffusion creep.

501 **4.2 Geological Implications**

502 Similar to those for the Madoc dolomite by *Davis et al. [2008]*, our experimental
503 results for the Fangshan dolomite can also be used to describe the flow laws for crystal-
504 plastic deformation at low temperatures with an exponential relationship and
505 dislocation creep at high temperatures with a power relationship. In contrast to a higher
506 stress exponent $n=7$ assumed by *Davis et al. [2008]* and a much lower activation energy
507 $Q=145$ kJ/mol determined by *Holyoke et al. [2013]* both for dislocation creep, our stress
508 exponent ($n=4.75$) and activation energy ($Q=436$ kJ/mol) values are more reasonable
509 and reliable. In order to predict the deformation mechanisms dominating the rheology
510 of medium-grained dolomite aggregates within the Earth, the low temperature
511 exponential law and high temperature dislocation flow law determined in this study and
512 that reported for diffusion creep of fine-grained synthetic dolomite aggregates [*Davis*
513 *et al., 2008*] are combined to define a deformation mechanism map for dolomite
514 aggregate with a grain size of 100 μm in the logarithm stress versus T/T_m space (*Figure*
515 *12*), where T_m is the melting point of dolomite [*Wyllie and Huang, 1976*]. As the
516 activation energy in our power law for dislocation creep is quite close to the value of
517 *Davis et al. [2008]* but much higher than that of *Holyoke et al. [2013]*, our deformation
518 mechanism map is similar to that of *Davis et al. [2008]* but apparently different from
519 that of *Holyoke et al. [2013]*. Compared with the map of *Davis et al. [2008]*, a little
520 steeper dislocation creep-diffusion creep boundary is displayed in our map due to
521 relatively more sensitive temperature dependence of strength for Fangshan dolomite
522 than Madoc dolomite. As shown in *Figure 12*, three fields are distinct in the deformation
523 mechanism map for dolomite with LTP at high stresses, dislocation creep at high
524 temperatures and relatively high stresses, and diffusion creep at low stresses and
525 elevated temperatures. Crystal plasticity and twinning dominate the deformation of
526 dolomite at very high stresses, nearly independent on strain rate. From laboratory to
527 nature, for instance, several orders of magnitude difference in strain rate does not result
528 in a large difference in strength in the field of LTP. In addition, strengths increase
529 slightly with increasing temperature in this field, corresponding to the thermal increase

530 in CRSS of c-slip [Figure 11; Barber et al., 1981]. This is unusual relative to generally
531 accepted temperature dependence of strength for common rock-forming minerals
532 although such thermal hardening was earlier reported by Davis et al. [2008] for Madoc
533 dolomite deformed at $T \leq 700$ °C, by Higgs and Handin [1959] and Barber et al. [1981]
534 for oriented single crystals of dolomite, and by some much earlier works [e.g., Ardley,
535 1955; Davies and Stoloff, 1965; Lawley et al., 1961; Stoloff and Davies, 1964] for alloys
536 with order-disorder or lattice anisotropy. One possible interpretation by Barber et al.
537 [1981] is that the thermal hardening is limited to basal (c) slip and during dislocation
538 movement the increase of friction of CO_3^{2-} groups increases with thermal vibration,
539 expansion and rotation of CO_3^{2-} groups. However, there is no similar thermal hardening
540 found in calcite [e.g., Barber et al., 1981, 2007; de Bresser and Spiers, 1997] with
541 crystal structure similar to dolomite. Therefore, further research is needed to explore
542 the reasons behind this behavior.

543 Extrapolated to nature, for dolomite aggregates with a grain size of 100 μm
544 deformed over most geological strain rates (10^{-10} - 10^{-14} s^{-1}), LTP dominates at
545 temperatures not higher than ~ 560 °C. At temperatures between 560 °C and 650 °C, the
546 deformation of dolomites is dominated by LTP at relatively high differential stresses
547 and by diffusion creep at low stresses (Figure 12a). When $T > 650$ °C, however, diffusion
548 creep is the dominant deformation mechanism, likely accompanied by small amount of
549 LTP and dislocation creep deformation. Given a specific strain rate (10^{-14} s^{-1}) for the
550 deformation of dolomite in nature, change in grain size shifts the diffusion creep-
551 dislocation creep boundary to higher temperatures when coarsening or to lower
552 temperatures when refining (Figure 12b). Depending on grain size, the extent of the
553 dislocation creep field is limited to high temperatures and relatively high stresses
554 ($T > \sim 460$ °C for $d = 1$ μm , $T > \sim 500$ °C for $d = 10$ μm , $T > \sim 560$ °C for $d = 100$ μm , and
555 $T > \sim 600$ °C for $d = 250$ μm). This means that dislocation creep is expected to occur in
556 relatively narrow space undergoing high stresses and high temperatures, instead
557 diffusion creep is expected to dominate the deformation of dolomite over most
558 geological strain rates and low tectonic stress environments.

559

560 **5. Conclusions**

561 Triaxial compression experiments performed on medium-grained Fangshan
562 dolomites at effective pressures of ~50-300 MPa, temperatures of 27-900 °C, and strain
563 rates from 10^{-6} s^{-1} to $2 \times 10^{-4} \text{ s}^{-1}$ roughly define three different deformation regimes:
564 regime 1 dominated by LTP (dislocation slip and f-twinning), regime 2 by dislocation
565 creep, and regime 3 by transient state of LTP to dislocation creep. Mechanical data are
566 used to determine the rheological parameters of LTP by an exponential relationship with
567 $\alpha = 0.081 \pm 0.0083$ and $\ln \dot{\epsilon}_0 = -76.66 \pm 6.24$ and of dislocation creep by a power law
568 relationship with $n = 4.75 \pm 0.58$, $Q = 436 \pm 54 \text{ kJ/mol}$ and $\log A = 3.48 \pm 1.41$.

569 Compared with previous studies, our medium-grained Fangshan dolomites show
570 similar rheological behavior to coarse-grained Madoc dolomites but have a beginning
571 temperature of dislocation creep about 50-100 °C lower than the latter. In addition, a
572 more reasonable activation energy, higher than those for diffusion creep of fine-grained
573 dolomites determined previously, is obtained for the medium-grained Fangshan
574 dolomite. Flow laws for medium-grained Fangshan dolomite determined in this study
575 and fine-grained synthetic dolomite reported previously are combined to construct a
576 deformation mechanism map for dolomite. Three fields are distinguished with LTP at
577 high stresses and low temperature, dislocation creep at high temperatures and relatively
578 high applied stresses, and diffusion creep at moderate-high temperatures and low
579 stresses. The dislocation creep-diffusion creep boundary shifts to higher temperatures
580 when coarsening or to lower temperatures when refining. Dislocation creep is expected
581 to occur in a relatively narrow space undergoing high temperatures and high stresses,
582 instead diffusion creep is expected to dominate the deformation of dolomite in tectonic
583 settings characterized by most geological strain rates and low stress.

584

585 **Acknowledgement**

586 We appreciate the critical and constructive comments of the reviewers and the
587 Editor-in-Chief that helped us to improve the manuscript. Dr. Hao Wang is thanked for
588 helping in fielding work and Dr. Guinan Zhang is thanked for help during some

589 experiments. Professor Yongsheng Zhou is gratefully acknowledged for critical
590 comments on an early version of this manuscript. The data supporting the analysis and
591 conclusions is given in Figures and Tables. Original data is accessible through the
592 Mendeley repository (<http://dx.doi.org/10.17632/hmmt2797yk.1>). This work was supported by
593 the Strategic Priority Research Program (B) of Chinese Academy of Sciences (Grant
594 No. XDB18010402), the National Natural Science Foundation of China (Grant Nos.
595 41572198 and 41702224), and the Pearl River Talent Plan of Guangdong Province. This
596 is a contribution to No. IS-XXXX from the GIGCAS.

597

598 **References**

599 Ardley, G. W. (1955), On the effect of ordering upon the strength of Cu_3Au , *Acta*
600 *Metall.*, 3, 525-532.

601 Austin, N., and B. Evans (2009), The kinetics of microstructural evolution during
602 deformation of calcite, *J. Geophys. Res.*, 114, B09402,
603 doi:10.1029/2008JB006138.

604 Austin, N. J., and L. A. Kennedy (2005), Textural controls on the brittle deformation
605 of dolomite: variations in peak strength, In: Gapais, D., Brun, J.P., Cobbold, P.R.
606 (Eds.), *Deformation Mechanisms, Rheology and Tectonics: from Minerals to the*
607 *Lithosphere, Spec. Publ. Geol. Soc. Lond.*, 243, 37–49.

608 Austin, N. J., L. A. Kennedy, J. M. Logan, and R. Rodway (2005), Textural controls on
609 the brittle deformation of dolomite: the transition from brittle faulting to cataclastic
610 flow, In: Gapais, D., Brun, J.P., Cobbold, P.R. (Eds.), *Deformation Mechanisms,*
611 *Rheology and Tectonics: from Minerals to the Lithosphere, Spec. Publ. Geol. Soc.*
612 *Lond.*, 243, 51–66.

613 Barber, D. J., H. C. Heard, and H. R. Wenk (1981), Deformation of dolomite single
614 crystals from 20 °C -800 °C, *Phys. Chem. Miner.*, 7, 271–286.

615 Barber, D. J., and H. R. Wenk (1979), Deformation twinning in calcite, dolomite, and
616 other rhombohedral carbonates, *Phys. Chem. Miner.*, 5, 141-165.

617 Barber, D. J., and H. R. Wenk (2001), Slip and dislocation behavior in dolomite, *Eur.*
618 *J. Mineral.*, 13, 221–243.

619 Barber, D. J., H. R. Wenk, J. Gomez-Barreiro, E. Rybacki, and G. Dresen (2007), Basal
620 slip and texture development in calcite: new results from torsion experiments,
621 *Phys. Chem. Miner.*, *34*, 73-84.

622 Barber, D. J., H. R. Wenk, and H. C. Heard (1994), The plastic deformation of
623 polycrystalline dolomite: comparison of experimental results of theoretical
624 predictions, *Mater. Sci. Eng. A*, *175*, 83–104.

625 Bass, J. D. (1995), Elasticity of minerals, glasses and melts. In: Ahrens, T.J. (Ed.),
626 Mineral Physics and Crystallography, A Handbook of Physical Constants, AGU.,
627 Washington, D.C., pp. 45–63.

628 Bestmann, M., K. Kunze, and A. Matthews (2000), Evolution of a calcite marble shear
629 zone complex on Thassos Island, Greece: microstructural and textural fabrics and
630 their kinematic significance, *J. Struct. Geol.*, *22*, 1789–1807.

631 Davis, N. E., A. K. Kronenberg, and J. Newman (2008), Plasticity and diffusion creep
632 of dolomite, *Tectonophysics*, *456*, 127–146.

633 Davis, R. G., and N. S. Stoloff (1965), On the yield stress of aged Ni-Al alloys, *Trans.*
634 *Metall. Soc. AIME.*, *233*, 714-719.

635 de Bresser, J. H. P. (2002), On the mechanism of dislocation creep of calcite at high
636 temperature: Inferences from experimentally measured pressure sensitivity and
637 strain rate sensitivity of flow stress, *J. Geophys. Res.* *107*, 1–16.

638 de Bresser, J. H. P., and C. J. Spiers (1997), Strength characteristics of the r, f, and c
639 slip systems in calcite, *Tectonophysics*, *272*, 1-23.

640 de Bresser, J. H. P., J. L. Urai, and D. L. Olgaard (2005), Effect of water on the strength
641 and microstructure of Carrara marble axially compressed at high temperature, *J.*
642 *Struct. Geol.*, *27*(2), 265-281.

643 Delle Piane, C., L. Burlini, K. Kunze, P. Brack, and J. P. Burg (2008), Rheology of
644 dolomite: large strain torsion experiments and natural examples, *J. Struct. Geol.*,
645 *30*, 767–776.

646 Freund, D., Z. C. Wang, E. Rybacki, and D. Georg (2004), High-temperature creep of
647 synthetic calcite aggregates: influence of Mn-content, *Earth Planet. Sci. Lett.*,
648 *226*(3-4), 433-448.

649 Goldsmith, J. R. (1959), Some aspects of the geochemistry of carbonates, In: Abelson,
650 P.H. (Ed.), *Researches in Geochemistry*, vol. 1, pp. 336–358.

651 Goto, A., K. Kunugiza, and S. Omori (2007), Evolving fluid composition during
652 prograde metamorphism in subduction zones: A new approach using carbonate-
653 bearing assemblages in the pelitic system, *Gondwana Res.*, 11(1-2), 166-179.

654 Gratier, J. P., J. Richard, F. Renard, et al., (2011), A seismic sliding of active faults by
655 pressure solution creep: evidence from the San Andreas Fault Observatory at
656 Depth, *Geology*, 39(12), 1131-1134.

657 Griggs, D., and W. B. Miller (1951), Deformation of Yule marble, part I. Compression
658 and extension on dry Yule marble at 10000 atmospheres confining pressure, room
659 temperature, *GSA Bulletin*, 62, 853–862.

660 Griggs, D. T., F. J. Turner, I. Borg, and J. Sosoka (1953), Deformation of Yule marble,
661 part V., effects at 300 °C, *GSA Bulletin*, 64, 1327-1342.

662 Handin, J., and H. W. Fairbairn (1955), Experimental deformation of Hasmark dolomite,
663 *GSA Bulletin*, 66, 1257-1274.

664 Handin, J., and D. Griggs (1951), Deformation of Yule marble, Part II., Predicted fabric
665 changes, *GSA Bulletin*, 62, 863-886.

666 Heard, H. C. (1976), Comparison of the flow properties of rocks at crustal conditions,
667 *Philosophical Transactions of the Royal Society of London*, 283, 173-186.

668 Heard, H. C., and C. B. Raleigh (1972), Steady-state flow in marble at 500 ° to 800 °C,
669 *GSA Bulletin*, 83, 935–956.

670 Herwegh, M., X. Xiao, and B. Evans (2003), The effect of dissolved magnesium on
671 diffusion creep in calcite, *Earth Planet. Sci. Lett.*, 212(3), 457-470.

672 Herwegh, M., J. H. P. de Bresser, and J. H. ter Heege (2005), Combining natural
673 microstructures with composite flow laws: an improved approach for the
674 extrapolation of lab data to nature, *J. Struct. Geol.*, 27, 503-521.

675 Higgs, D. V., and J. Handin (1959), Experimental deformation of dolomite single
676 crystals, *GSA Bulletin*, 70, 245–278.

677 Holyoke, C. W., A. K. Kronenberg, and J. Newman (2013), Dislocation creep of
678 polycrystalline dolomite, *Tectonophysics*, 590, 72-82.

679 Holyoke, C. W., A. K. Kronenberg, J. Newman, and C. Ulrich (2014), Rheology of
680 magnesite, *J. Geophys. Res.*, *119*, 6534-6557.

681 Karato, S. (2008), Deformation of Earth Materials: An Introduction to the Rheology of
682 Solid Earth, *Cambridge University Press*, 463.

683 Lawley, A., E. A. Vidoz, and R. W. Cahn (1961), The dependence of the flow stress of
684 Fe₃Al on crystallographic order, *Acta Metall.*, *9*, 287-296.

685 Li, J. F., M. S. Song, T. B. Shao, Y. Xia, Q. Wang, and W. Zhou (2013), Correction for
686 the axial deformation data recorded by Paterson-type gas medium high-pressure
687 high temperature machine, *Geotectonica et Metallogenia*, *37*(1), 127-137 (in
688 Chinese with English abstract).

689 Neumann, E.-R. (1969), Experimental recrystallization of dolomite and comparison of
690 preferred orientations of calcite and dolomite in deformed rocks, *J. Geol.*, *77*, 426-
691 438.

692 Paterson, M. S. (1970), A high-pressure, high-temperature apparatus for rock
693 deformation, *International Journal of Rock Mechanics & Mining Science &*
694 *Geomechanics Abstracts*, *7*(5), 517-526.

695 Poirier, J. P. (1985), Creep of Crystals: High-Temperature Deformation Processes in
696 Metals, Ceramics, and Minerals. *Cambridge University Press*, Cambridge, 260pp.

697 Renner, J., B. Evans, and G. Siddiqi (2002), Dislocation creep of calcite, *J. Geophys.*
698 *Res.*, *107*, 1-16.

699 Rutter, E. H. (1972), Influence of interstitial water on rheological behavior of calcite
700 rocks, *Tectonophysics*, *14*, 13–33.

701 Rutter, E. H. (1974), Influence of temperature, strain rate and interstitial water in
702 experimental deformation of calcite rocks, *Tectonophysics*, *22*, 311–334.

703 Rybacki, E., C. Janssen, R. Wirth, K. Chen, H.-R. Wenk, D. Stromeier, and G. Dresen
704 (2011), Low-temperature deformation in calcite veins of SAFOD core samples
705 (San Andreas Fault)-Microstructural analysis and implications for fault rheology,
706 *Tectonophysics*, *509*(1-2), 107-119.

707 Rybacki, E., B. Evan, C. Janssen, R. Wirth, and G. Dresen (2013), Influence of stress,
708 temperature, and strain on calcite twins constrained by deformation experiments,

709 *Tectonophysics*, 601, 20-36.

710 Schmid, S., J. N. Boland, and M. S. Paterson (1977), Super-plastic flow in fine-grained
711 limestone, *Tectonophysics*, 43, 257–292.

712 Schmid, S., M. S. Paterson, and J. N. Boland (1980), High temperature flow and
713 dynamic recrystallization in Carrara marble, *Tectonophysics*, 65, 245–280.

714 Shao, T.B, S. C. Ji, J. F. Li, Q. Wang, and M. S. Song (2011), Paterson gas-medium
715 high-pressure high-temperature testing system and its applications in rheology of
716 rocks, *Geotectonica et Metallogenia*, 35(3), 457-476 (in Chinese with English
717 abstract).

718 Song, M. S., T. B. Shao, J. F. Li, S. C. Ji, and Q. Wang (2014), Experimental study of
719 deformation of Carrara marble at high pressure and high temperature, *Acta
720 Petrologica Sinica*, 30(2), 589-596 (in Chinese with English abstract).

721 Stoloff, N. S., and R. G. Davies (1964), The effect of ordering on the plastic
722 deformation of Mg₃Cd, *Trans. Am. Soc. Met.*, 57, 247-260.

723 Turner, F. J., D. T. Griggs, R. H. Clark, and R. H. Dixon (1956), Deformation of Yule
724 marble, part VII: development of oriented fabrics at 300 °C-500 °C, *GSA Bulletin*,
725 67, 1259–1294.

726 Turner, F. J., D. T. Griggs, H. Heard, and L. W. Weiss (1954), Plastic deformation of
727 dolomite rock at 380 °C, *Am. J. Sci.*, 252, 477–488.

728 Ulrich, S., K. Schumann, and M. Casey (2002), Microstructural evolution and
729 rheological behavior of marbles deformed at different crustal levels, *J. Struct.
730 Geol.*, 24, 979-995.

731 Walker, A. N., E. H. Rutter, and K. H. Brodie (1990), Experimental study of grain-size
732 sensitive flow of synthetic, hot-pressed calcite rocks, In: Knipe, R.J., Rutter, E.H.
733 (Eds.), Deformation Mechanisms, Rheology and Tectonics, *Spec. Publ. Geol. Soc.*,
734 54, 259–284.

735 Wright, R. N. (2016), Chapter 11 – Mechanical Properties of Wire and Related Testing,
736 in Wire Technology (Second Edition), *Process Engineering and Metallurgy*, 129-
737 157.

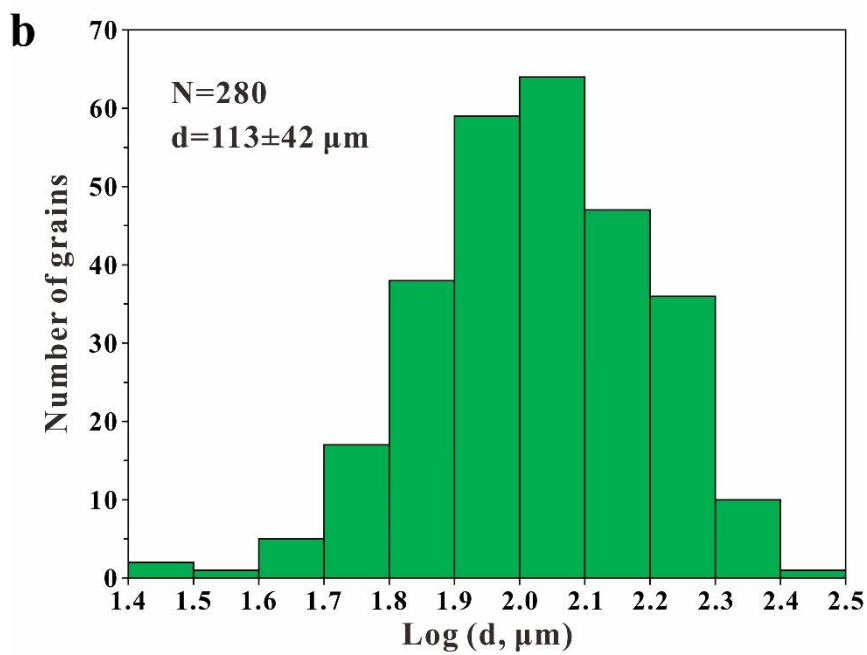
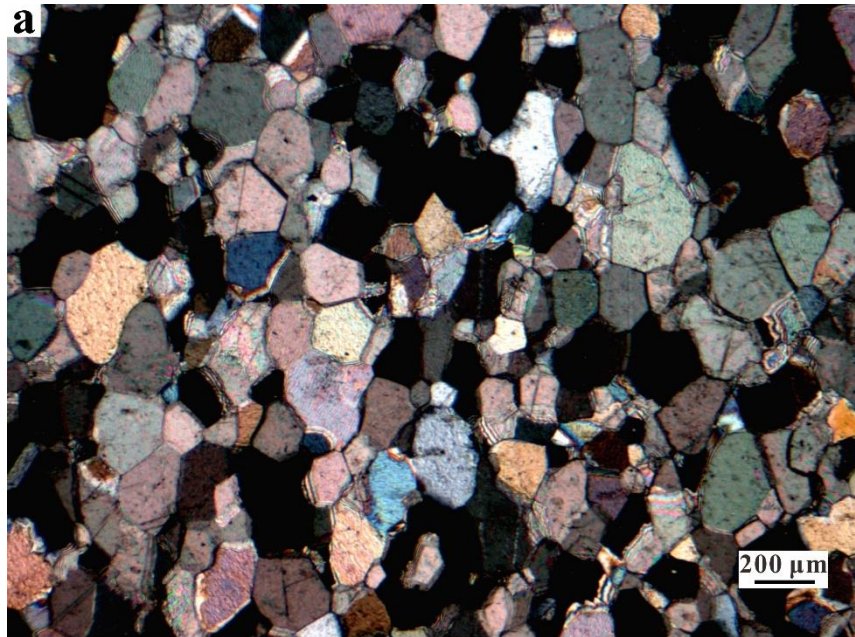
738 Wyllie, P. J. and W. L. Huang (1976), Carbonation and melting reactions in the system

- 739 CaO-MgO-SiO₂-CO₂ at mantle pressures with geophysical and petrological
740 applications, *Contrib. Miner. Petrol.*, 54, 79-107.
- 741 Xu, L. L., and B. Evans (2010), Strain heterogeneity in deformed Carrara marble using
742 a microscale strain mapping technique, *J. Geophys. Res.*, 115(B4), B04202.
- 743 Xu, L. L., J. Renner, M. Herwegh, and B. Evans (2009), The effect of dissolved
744 magnesium on creep of calcite II: transition from diffusion creep to dislocation
745 creep, *Contrib. Miner. Petrol.*, 157(3), 339-358.
- 746 Zhang, L., D. J. Ellis, R. J. Arculus, W. Jiang, and C. Wei (2003), 'Forbidden zone'
747 subduction of sediments to 150 km depth – The reaction of dolomite to magnesite
748 plus aragonite in the UHPM metapelites from western Tianshan, China, *J.*
749 *Metamorph. Geol.*, 21, 523-529.
- 750 Zhang, Y. H., Y. S. Zhou, W. M. Yao, C. R. He, and J. X. Dang (2017), Experimental
751 study on the effect of water on the strength and deformation mechanism of Carrara
752 marble at high temperature, *Seismology and Geology*, 39(1), doi:10.3969/
753 j.issn.0253-4967.2017.01 (in Chinese with English abstract).
- 754 Zhang, Y. Y., and Y. S. Zhou (2012), The strength and deformation mechanisms of
755 brittle-plastic transition zone, and the effects of strain rate and fluids, *Seismology*
756 *and Geology*, 34(1), 172-194 (in Chinese with English abstract).

757

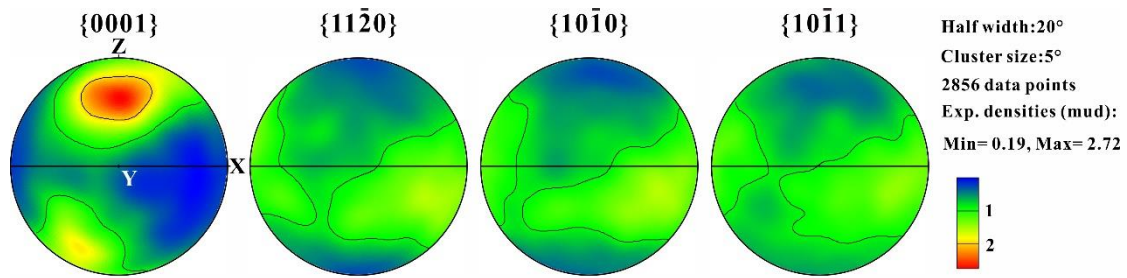
Figure captions

758



759

760 **Figure 1.** Orthogonal optical micrograph (a) and frequency diagram of grain diameter
761 (b) show that the starting materials (Fangshan dolomites) have approximately equant
762 grains with diameter $\sim 113 \mu\text{m}$ and are characterized by sharp grain boundaries,
763 uniform extinction, and some twin.



764

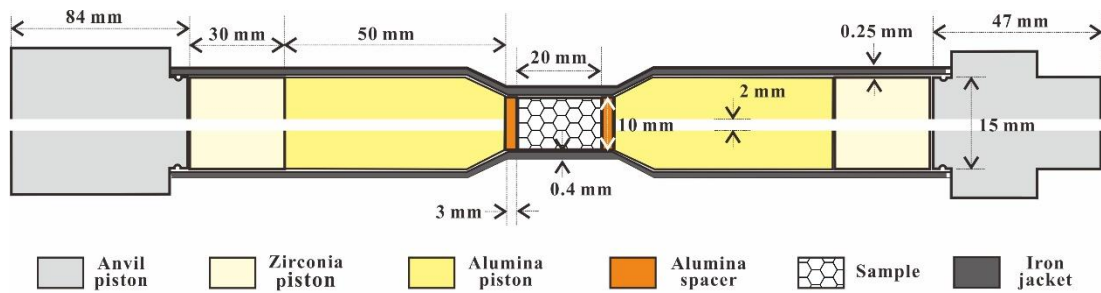
765 **Figure 2.** Pole figures of starting materials indicative of a weak fabric of c-axis

766

767

768

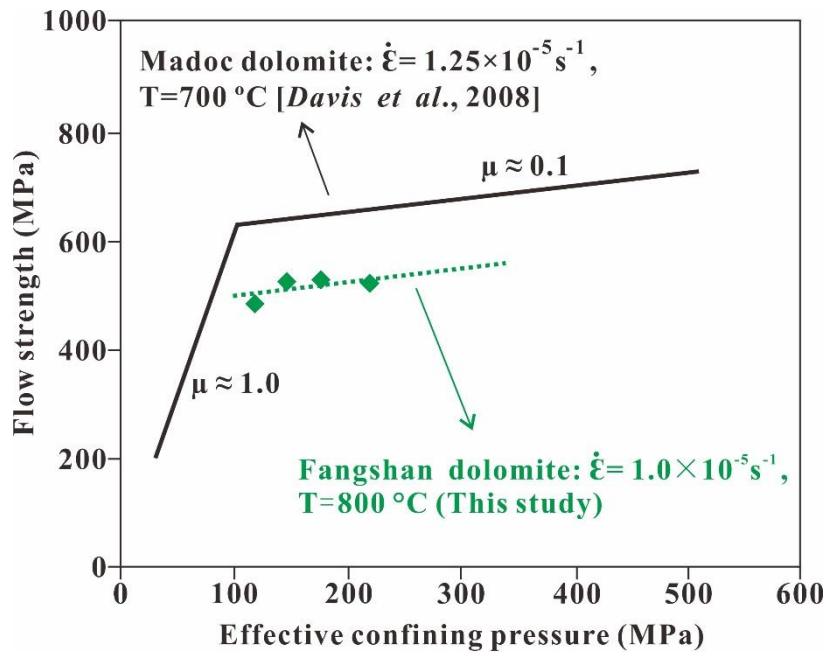
769



770

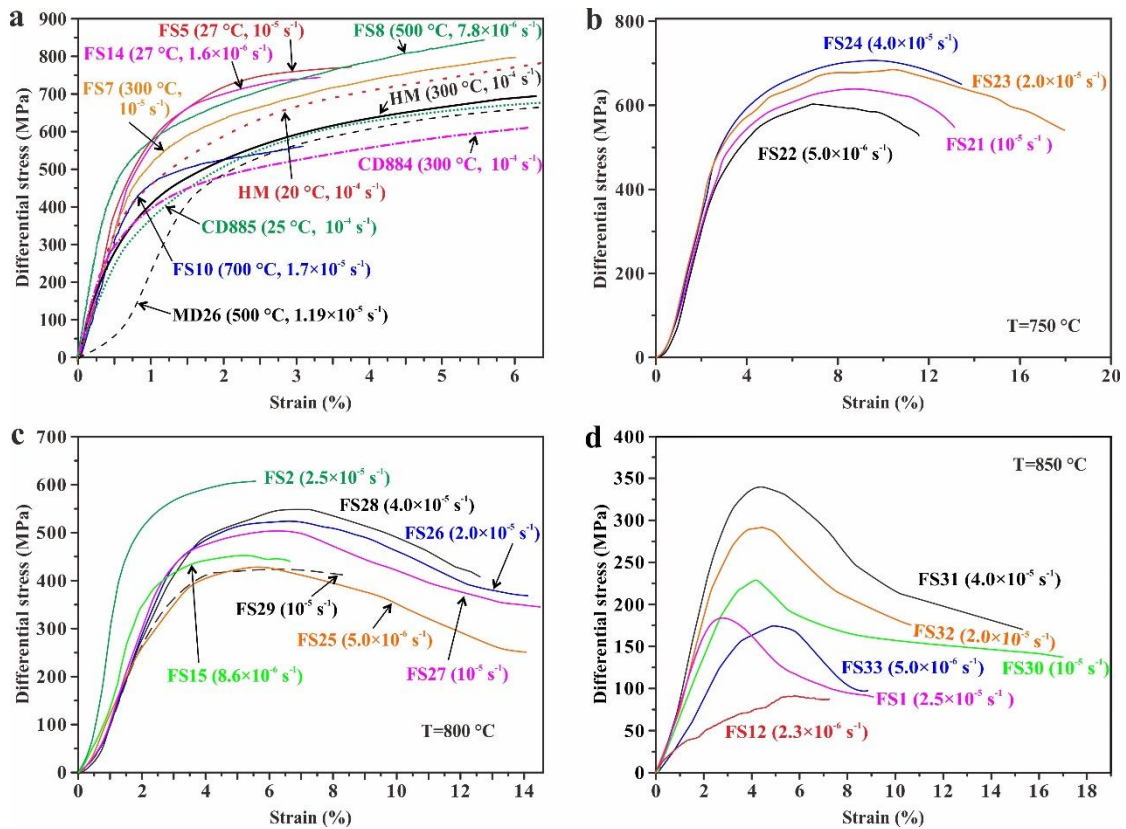
771 **Figure 3.** Schematic illustration of specimen assembly for triaxial compression

772 experiments in a Paterson-type deformation apparatus



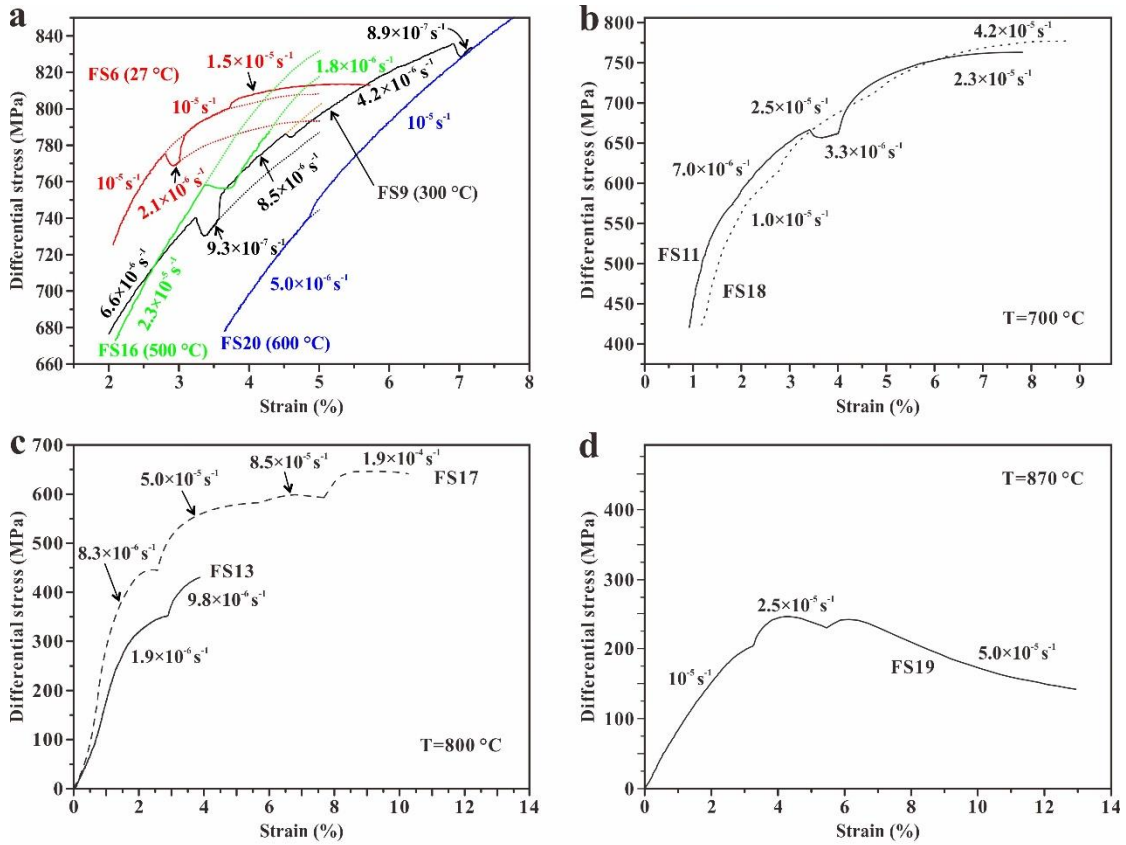
774

775 **Figure 4.** Effective pressure (P_e) dependence of flow strength of polycrystalline
 776 dolomite. Black lines are obtained by fitting flow strength to effective pressure of data
 777 on coarse-grained Madoc dolomite deformed at $700 \text{ }^\circ\text{C}$ and $1.25 \times 10^{-5} \text{ s}^{-1}$ from Davis
 778 *et al.* [2008]. Specifically, the flow strength of Madoc dolomite is linearly dependent
 779 on effective pressure with a tiny apparent coefficient of inner friction about 0.1 ($\mu \cong$
 780 0.1) if deformed at $P_e > 100 \text{ MPa}$, $700 \text{ }^\circ\text{C}$ and strain rate of $1.25 \times 10^{-5} \text{ s}^{-1}$, while if $P_e <$
 781 100 MPa the dependence of flow strength on effective pressure meets the Mohr –
 782 Coulumb Criterion with an apparent coefficient of inner friction about 1.0 ($\mu \cong 1.0$).
 783 Green diamonds represent the data of medium-grained Fangshan dolomite compressed
 784 at $800 \text{ }^\circ\text{C}$ and $1.0 \times 10^{-5} \text{ s}^{-1}$, to which a green line is fitted showing a weak dependence
 785 of flow strength on effective pressure with an apparent inner friction coefficient equal
 786 to 0.1.



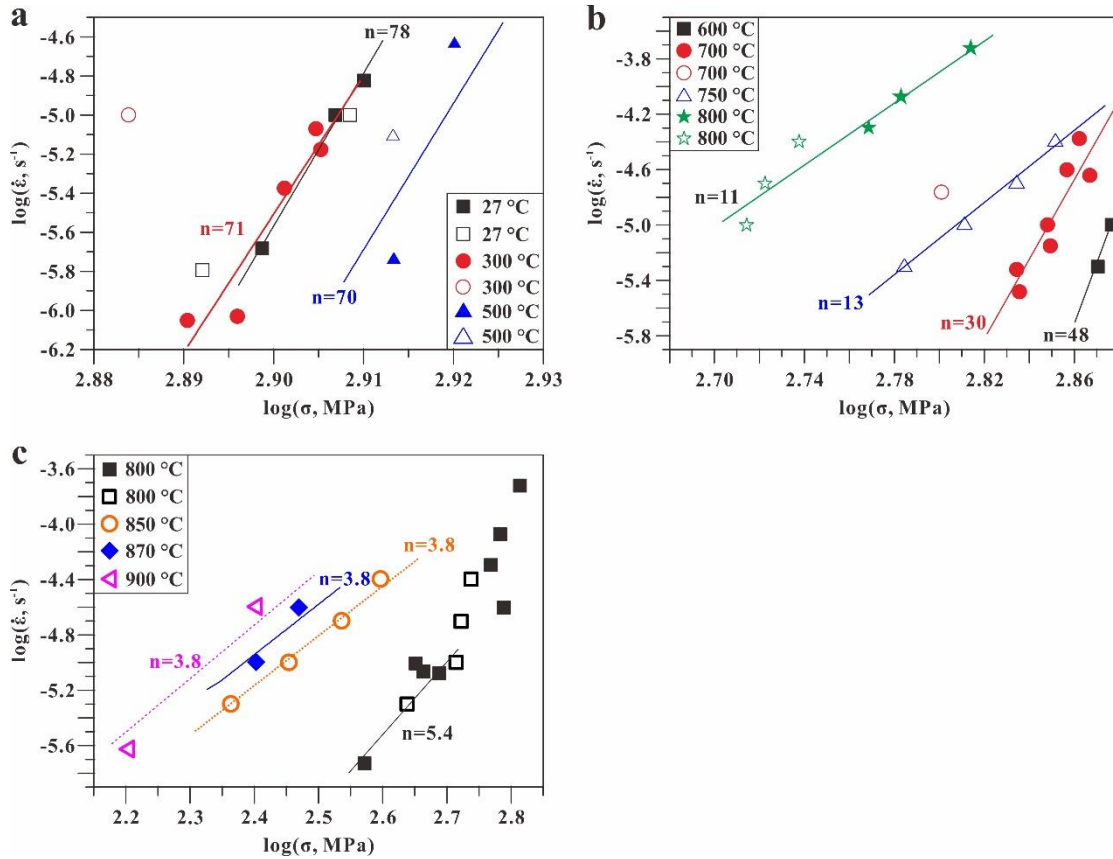
787

788 **Figure 5.** Differential stress versus strain curves of dolomite compressed at individual
 789 constant strain rates. HM, CD, and MD26 in Figure 5a are compilation of previous
 790 results for Hasmark dolomite [T-cylinders, *Handin and Fairbairn, 1955*], Crevola
 791 dolomite [*Barber et al., 1994*], and Madoc dolomite [*Davis et al., 2008*], respectively,
 792 obtained at a strain rate of 10^{-4} s^{-1} . The effective confining pressures for our all tests are
 793 50-300 MPa. Respective strain rate and temperature or alone strain rate at a constant
 794 temperature are marked after each sample name.



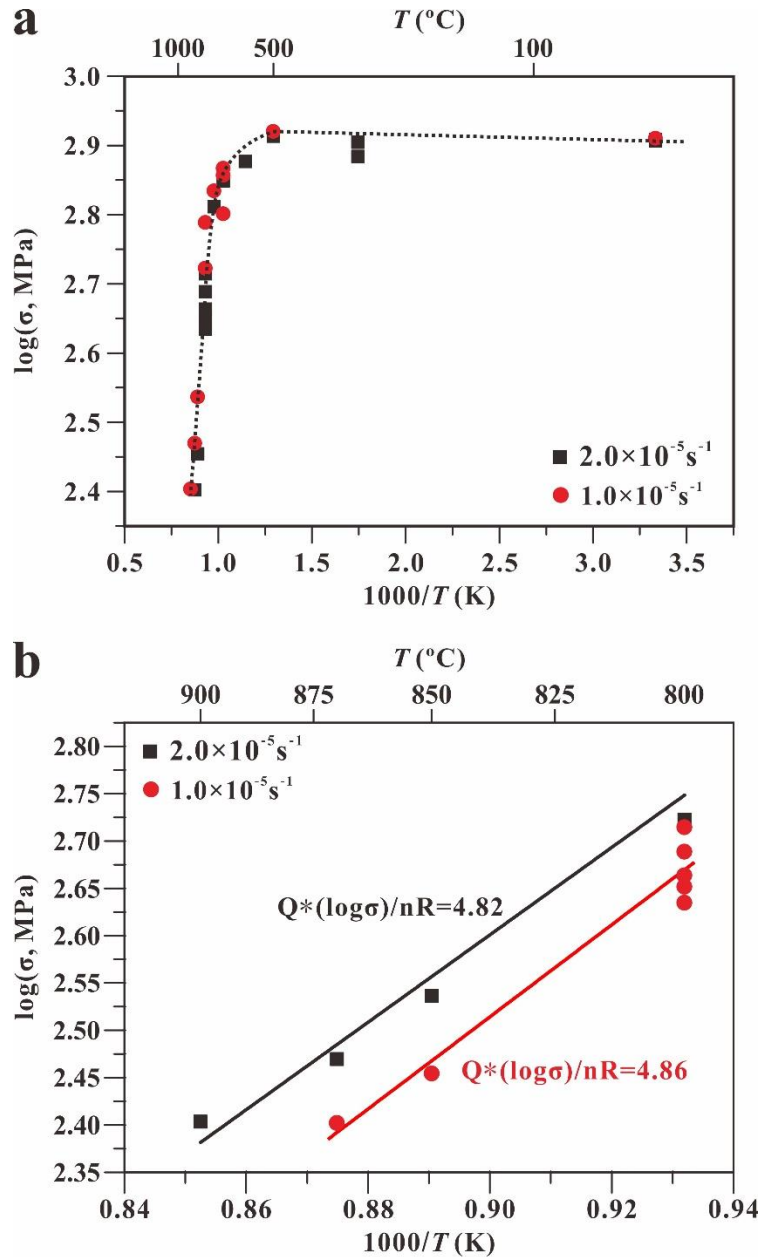
795

796 **Figure 6.** Differential stress versus strain curves of Fangshan dolomite compressed in
 797 strain-rate-stepping experiments. The effective confining pressures for all tests are 50-
 798 300 MPa. Strain rates are marked along or with arrows pointing to each stage of curve.
 799 In Figure a, curves of different samples (temperatures) are marked in different color,
 800 dotted line represents the extension of curve under a strain rate.



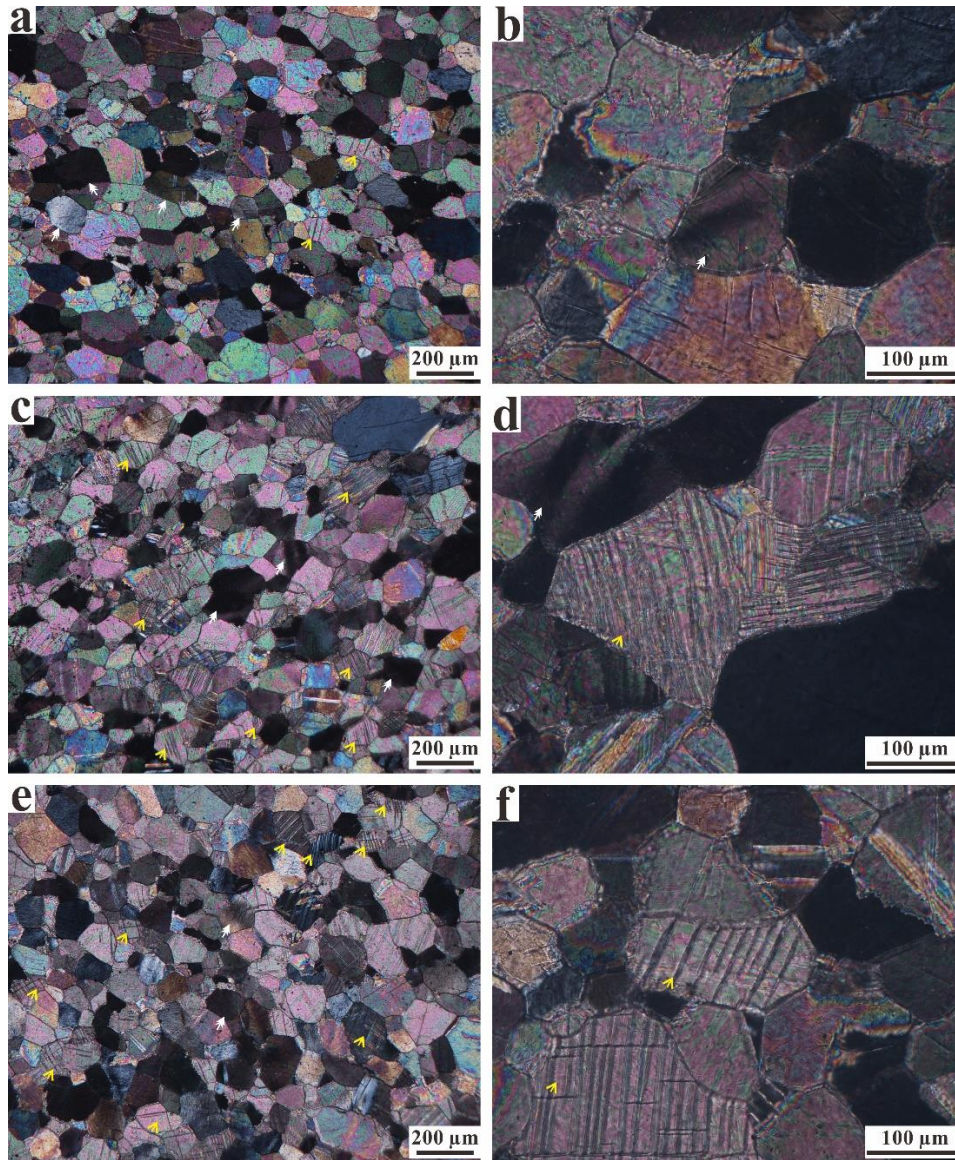
801

802 **Figure 7.** log $\dot{\epsilon}$ versus log σ plots for Fangshan dolomites deformed in three
803 regimes. Note: The confining pressures of all tests are 300 MPa. a – Regime 1 at
804 temperature $\leq 500^\circ\text{C}$ with extremely high stress exponents ($n \approx 70$), indicating
805 obviously weak dependence of flow strength on strain rate; b - Regime 3 at temperature
806 from 600 °C to 750 °C with moderate and gradually decreasing stress exponents (n
807 value of 48 to 13); c – Regime 2 at temperatures higher than 800°C and/or equal to 800
808 °C but with flow strength lower than 520 MPa is characterized by significantly low
809 stress exponents, whose values are basically consistent with those expected for
810 dislocation creep. Solid symbols represent data collected from strain-rate-stepping
811 experiments, while hollow symbols represent data collect from individual constant
812 strain rate tests.

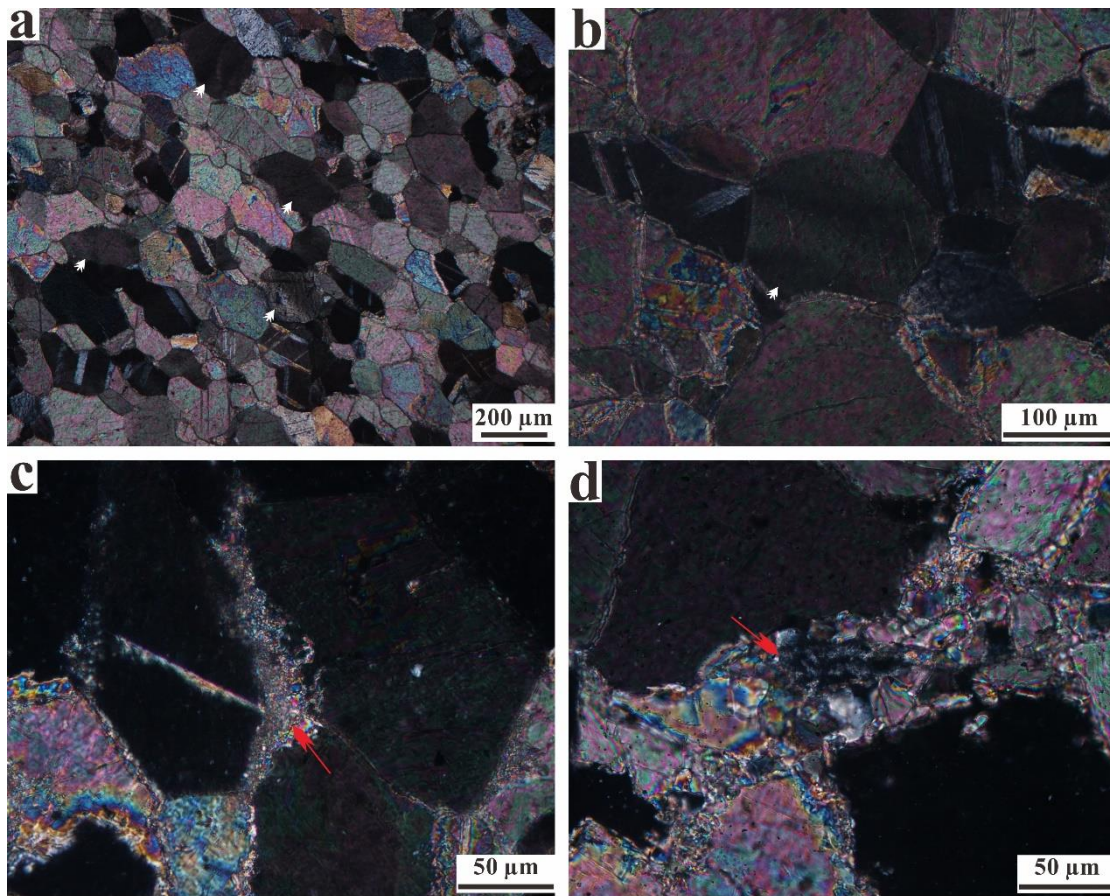


813

814 **Figure 8.** $\log\sigma$ versus $1000/T$ plots of experimental results displaying strength of
 815 medium-grained Fangshan dolomite as a function of temperature. (a) At low
 816 temperatures (≤ 500 °C), strengths of medium-grained Fangshan dolomite are
 817 insensitive to temperature and increase very slightly with increasing temperature. At
 818 moderate temperatures (500 °C $< T < \sim 750$ °C), strengths are much more insensitive to
 819 temperature and decrease significantly with increasing temperature. At high
 820 temperatures ($\geq \sim 750$ °C), strengths decrease sharply with increasing temperature. (b)
 821 At higher temperatures (800 °C $\leq T \leq 900$ °C), fittings of $\log\sigma$ versus $1000/T$ at two
 822 different strain rates result in a similar slope given by $Q^*(\log\sigma)/nR=4.8$.

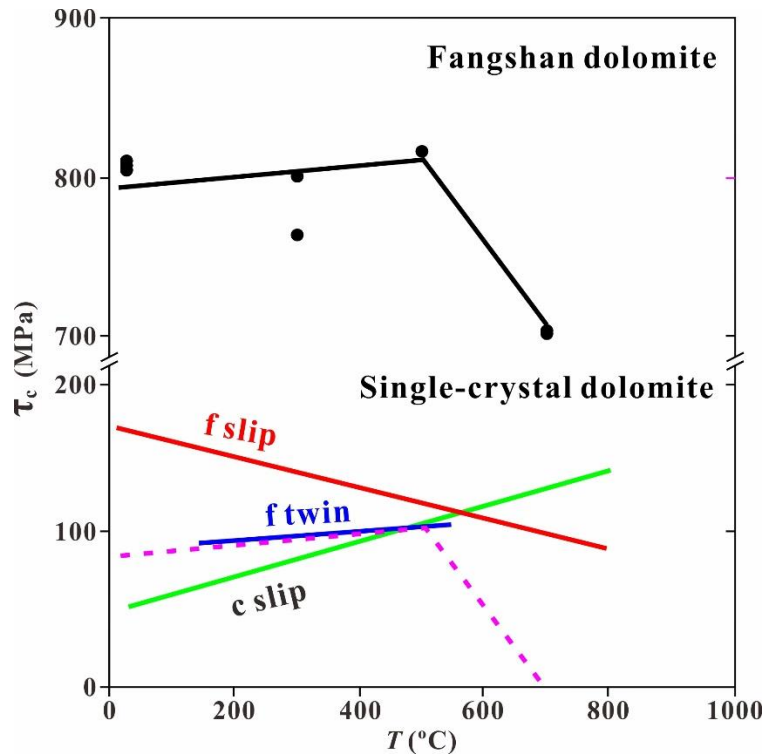


823
 824 **Figure 9.** Optical microstructures of medium-grained Fangshan dolomite, deformed at
 825 temperatures ≤ 500 °C, in cross-polarized light. (a and b) Undulatory extinction and
 826 extinction bands developed in the Fangshan dolomite deformed at room temperature;
 827 (a) sample FS14 deformed at room temperature and a constant strain rate of $1.6 \times 10^{-6} \text{ s}^{-1}$
 828 1 to a total strain of 3.65; (b) sample FS6 deformed at room temperature and stepping
 829 strain rates to a total strain of 6.29%. (c and d) Both undulatory extinction and f – twins
 830 were pervasive in the Fangshan dolomites (sample FS9) deformed at 300 °C and
 831 stepping strain rates to a total strain of 7.18% (e and f) f twinning became dominant in
 832 the Fangshan dolomites (sample FS8) at 500 °C and $7.8 \times 10^{-6} \text{ s}^{-1}$ to a total strain of 7%.
 833 The undulatory extinctions were represented by white arrows, while mechanical twins
 834 were marked by yellow arrows.



836

837 **Figure 10.** Optical microstructures of medium-grained Fangshan dolomite, deformed
 838 at temperatures ≥ 700 °C, in cross-polarized light. (a and b) Smooth undulating
 839 extinctions developed in the Fangshan dolomites (sample FS15) deformed at
 840 temperature ≥ 800 °C and stepping strain rates to a total strain of 11.1%. (c and d) Some
 841 new fine grains were discovered at the triple junction of dolomite grains or surrounding
 842 the accessory minerals such as mica and apatite in samples FS15 (c) and FS12 (d), the
 843 latter of which were deformed at 900 °C and $2.3 \times 10^{-6} \text{ s}^{-1}$ to a total strain of 7.27%. The
 844 undulatory extinctions were represented by white arrows, while the new fine grains
 845 formed by decomposition of dolomite were marked by red arrows.



846

847 **Figure 11.** Critical resolved shear stress (CRSS) for dominant slip and twin systems in
 848 single-crystal dolomite [Barber *et al.*, 1981] and polycrystalline Fangshan dolomites.

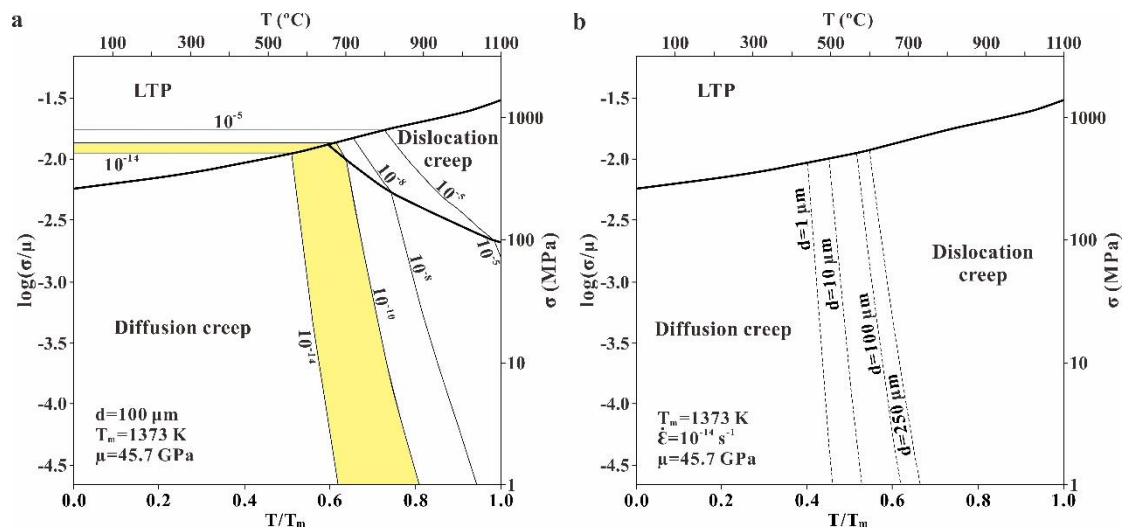
849 The temperature dependence trends of flow strength of the Fangshan dolomite were

850 consistent with a transition for single-crystal dolomite from c slip dominant at room

851 temperature to f twinning dominant at 500 °C, and then to dislocation creep dominant

852 deformation mechanism at temperature higher than 700 °C. Pink dotted line is formed

853 by the translation of the black solid line.



855

856 **Figure 12.** (a) A deformation mechanism map constructed using the low temperature
 857 plasticity (LTP) and dislocation creep flow laws of this study and the diffusion creep
 858 flow law of *Davis et al. [2008]* suggests that naturally-deformed, medium-grained
 859 ($100 \mu\text{m}$) dolomite aggregates deformed over most geological strain rates (10^{-10} - 10^{-14}
 860 s^{-1}), LTP dominates at temperatures not higher than $\sim 560 \text{ }^{\circ}\text{C}$. At temperatures between
 861 $560 \text{ }^{\circ}\text{C}$ and $650 \text{ }^{\circ}\text{C}$, the deformation of dolomites is dominated by LTP at relatively
 862 high differential stresses and by diffusion creep at low stresses. When $T > 650 \text{ }^{\circ}\text{C}$,
 863 however, diffusion creep is the dominant deformation mechanism, likely accompanied
 864 by LTP and dislocation creep accommodating very small amount strain. (b) Changing
 865 grain size of dolomite shifts the dislocation creep-diffusion creep boundary to lower
 866 temperatures when refining or to higher temperatures when coarsening. Temperature
 867 is normalized by a melting temperature [$T_m=1373 \text{ K}$, metastable extension from high
 868 pressure measurements, *Wyllie and Huang, 1976*], and flow strength is normalized by
 869 a shear modulus [$\mu=45.7 \text{ GPa}$, *Bass, 1995*].

Table 1. Chemical composition (wt.%) of Fangshan dolomite

Point#	MgO	CaO	FeO	Al ₂ O ₃	Na ₂ O	MnO	P ₂ O ₅	TiO ₂	Total	Mg/Ca
1	20.61	29.88	0.12	0.00	0.02	0.00	0.01	0.00	50.65	0.97
2	21.18	30.25	0.11	0.02	0.04	0.00	0.01	0.03	51.64	0.98
3	21.41	29.38	0.11	0.02	0.07	0.03	0.00	0.00	51.02	1.02

Table 2. Experimental conditions and mechanical results of constant strain rate tests on Fangshan dolomite

Run#	Confining pressure	Effective pressure	Temperature	Strain rate	Strain	Peak strength	Flow strength	Correctived by P_e	Total strian
	P_c	P_e			corresponding to peak strength				
	MPa	MPa	°C	sec ⁻¹	%	MPa	MPa		%
FS5	300	300	27	1.0×10^{-5}	3.0	783.82	810.00		3.1
FS14	300	300	27	1.6×10^{-6}		NA	780.00		3.7
FS7	300	300	300	1.0×10^{-5}		NA	765.35		6.4
FS8	300	300	500	7.8×10^{-6}		NA	819.01		7.0
FS10	300	270	700	1.7×10^{-5}		NA	629.48	632.48	3.5
FS21	300	250	750	1.0×10^{-5}	8.1	642.45		647.45	13.2
FS22	300	250	750	5.0×10^{-6}	7.1	603.74		608.74	11.6
FS23	300	250	750	2.0×10^{-5}	8.1	677.89		682.89	18.0
FS24	300	250	750	4.0×10^{-5}	9.6	705.53		710.53	13.5
FS2	300	220	800	2.5×10^{-5}	5.6	609.10	606.70	614.70	7.6
FS25	300	220	800	5.0×10^{-6}	5.9	426.48		434.48	14.1
FS26	300	220	800	2.0×10^{-5}	5.9	519.87		527.87	13.8
FS27	300	220	800	1.0×10^{-5}	5.4	509.98		517.98	14.5
FS28	300	220	800	4.0×10^{-5}	6.8	538.59		546.59	12.7
FS29	300	220	800	1.0×10^{-5}	6.0	423.18		431.18	9.8
FS30	260	60	850	1.0×10^{-5}	4.2	228.54		284.54	17.1
FS31	260	60	850	4.0×10^{-5}	4.4	339.28		395.28	15.1
FS32	260	60	850	2.0×10^{-5}	4.8	287.81		343.81	10.5
FS33	260	60	850	5.0×10^{-6}	5.0	175.12		231.12	9.5
FS1	300	50	900	2.5×10^{-5}	2.8	183.15	NA*	253.15	9.0
FS12	300	50	900	2.3×10^{-6}	5.8	90.05	83.63	160.05	7.3

*NA=Not achieved

Table 3. Experimental conditions and mechanical results of strain-rate-stepping tests on Fangshan dolomite

Run#	Confining pressure P_c MPa	Effective pressure P_e MPa	Temperature T °C	Strain rate sec^{-1}	Flow strength $\sigma_{5\%}$ MPa	Corrected by P_c MPa	Total strain ϵ_T %
FS6	300	300	27	1.0×10^{-5}	807.00		
				2.1×10^{-6}	792.00		
				1.0×10^{-5}	807.00		
				1.5×10^{-5}	812.96		6.3
FS9	300	300	300	6.6×10^{-6}	804.00		
				9.3×10^{-7}	787.00		
				8.5×10^{-6}	803.00		
				4.2×10^{-6}	796.54		
FS16	300	300	500	1.8×10^{-6}	819.14		
				2.3×10^{-5}	832.00		7.2
FS20	300		600	5.0×10^{-6}	742.17		
				1.0×10^{-5}	752.80		9.1
FS11	300	270	700	7.0×10^{-6}	704.00	707.00	
				3.3×10^{-6}	682.00	685.00	
				2.3×10^{-5}	733.12	736.12	9.4
FS18	300	270	700	4.8×10^{-6}	680.00	683.00	
				1.0×10^{-5}	702.00	705.00	
				2.5×10^{-5}	716.00	719.00	
				4.2×10^{-5}	725.25	728.25	
FS13	300	220	800	1.9×10^{-6}	365.00	373.00	
				9.8×10^{-6}	440.32	448.32	7.8
FS15	300	220	800	8.6×10^{-6}	452.66	460.66	
				3.1×10^{-6}	NA*		11.1
FS17	300	220	800	8.3×10^{-6}	480.00	488.00	
				5.1×10^{-5}	578.95	586.95	
				8.5×10^{-5}	598.72	606.72	6.8
				1.9×10^{-4}	643.56	651.56	8.8
FS19	300	70	870	1.0×10^{-5}	202.38	252.38	3.2
				2.5×10^{-5}	244.77	294.77	4.1
				5.0×10^{-5}	NA*		12.9
FS34	257	177	800	1.0×10^{-5}	515.70	523.7	
	227	147	800	1.0×10^{-5}	512.26	520.26	
	199	119	800	1.0×10^{-5}	472.44	480.44	

*NA=Not achieved